



**HAL**  
open science

## Engineering of perpendicular magnetic anisotropy in half-metallic magnetic Heusler epitaxial thin films

V. Palin, Charles Guillemard, C. de Melo, Sylvie Migot, P. Gargiani, M. Valvidares, F. Bertran, S. Andrieu

### ► To cite this version:

V. Palin, Charles Guillemard, C. de Melo, Sylvie Migot, P. Gargiani, et al.. Engineering of perpendicular magnetic anisotropy in half-metallic magnetic Heusler epitaxial thin films. *Physical Review Applied*, 2023, 20 (5), pp.054017. 10.1103/PhysRevApplied.20.054017 . hal-04592701

**HAL Id: hal-04592701**

**<https://hal.science/hal-04592701v1>**

Submitted on 18 Oct 2024

**HAL** is a multi-disciplinary open access archive for the deposit and dissemination of scientific research documents, whether they are published or not. The documents may come from teaching and research institutions in France or abroad, or from public or private research centers.

L'archive ouverte pluridisciplinaire **HAL**, est destinée au dépôt et à la diffusion de documents scientifiques de niveau recherche, publiés ou non, émanant des établissements d'enseignement et de recherche français ou étrangers, des laboratoires publics ou privés.


## Engineering of perpendicular magnetic anisotropy in half-metallic magnetic Heusler epitaxial thin films

V. Palin<sup>1,2</sup>, C. Guillemard<sup>3,†</sup>, C. de Melo<sup>1,‡</sup>, S. Migot<sup>1</sup>, P. Gargiani<sup>3</sup>, M. Valvidares<sup>3</sup>,  
F. Bertran<sup>2</sup>, and S. Andrieu<sup>1,\*</sup>

<sup>1</sup>*Institut Jean Lamour, Université de Lorraine/CNRS, UMR7198, Nancy 54011, France*

<sup>2</sup>*Synchrotron SOLEIL, L'Orme des Merisiers, Departementale 128, Saint-Aubin 91190, France*

<sup>3</sup>*ALBA Synchrotron, Cerdanyola del Vallès, Barcelona E-08290, Spain*

 (Received 10 July 2023; revised 8 September 2023; accepted 4 October 2023; published 7 November 2023)

Efficient spintronic devices based on thin films need a full spin polarization at Fermi energy, ultralow magnetic damping, and magnetization perpendicular to the film plane.  $\text{Co}_2\text{MnSi}$  and  $\text{Co}_2\text{MnGe}$  half-metal magnets Heusler compounds are good candidates due to their minority spin gap that leads to fully polarized current and ultralow magnetic damping. However, their low magnetocrystalline anisotropy leads to in-plane magnetization. One way to get perpendicular magnetic anisotropy in such Heusler compounds is to grow them on  $\text{Mn}_x\text{Ga}$ - or  $\text{Mn}_x\text{Ge}$ -buffer layers with the  $\text{D0}_{22}$  structure for which a strong magnetocrystalline anisotropy was reported. Here we first analyzed the impact of the stoichiometry of these binary alloys on their magnetic properties where the largest magnetocrystalline anisotropy was observed for the 3:1 stoichiometry. The replication of this perpendicular magnetic anisotropy in several half-metal magnet Heusler compounds epitaxially grown on top of them was thus analyzed by using standard magnetometry but also x-ray magnetic circular dichroism and *in situ* magneto-optic Kerr effect measurements. Squared hysteresis loops needed for applications were obtained using  $\text{Mn}_3\text{Ge}$  with a coercive magnetic field that can be tailored by varying the different thicknesses in the stack. Our results also allowed us to explain some reported magneto-optic Kerr effect results not yet understood.

DOI: [10.1103/PhysRevApplied.20.054017](https://doi.org/10.1103/PhysRevApplied.20.054017)

### I. INTRODUCTION

Magnetic random access memories (MRAMs) have been in the market since 2006 but have trouble to impose themselves as recording media in our daily computers. Nowadays, hard drive disks (HDDs) and solid-state drives (SSDs) are still commonly used. Despite the huge progress made in the spintronic field with spin-transfer torque and spin-orbit torque MRAM (STT and SOT MRAM) the development of alternative materials with more suitable properties to ensure the viability of these devices is still ongoing. The main challenges that physicists have to overcome are the following. First, a high Curie temperature is mandatory to implement the ferromagnetic layer in our daily devices. Second, a full spin polarization at the Fermi energy ensures that all the electrons (either spin up or spin down) are going to participate to the polarization of the current without any loss, and consequently increase the devices efficiency. Third, a low Gilbert magnetic damping

coefficient  $\alpha$  is needed to facilitate the magnetization reversal in devices. Fourth, a magnetization perpendicular to the thin-film surface is preferred since it reduces the needed current to switch the magnetization compared to in-plane magnetization and also allows the device size to be decreased by pushing back the superparamagnetic limit. Moreover, perpendicular magnetic anisotropy (PMA) thin films are ideal two-state devices, offering stable and distinct magnetization orientations for reliable information storage and processing.

Materials exhibiting a full spin polarization at the Fermi energy exist and are named half-metal magnets (HMMs). This property comes from an asymmetry in the density of state. For one spin channel, states are available at the Fermi energy while a gap is present for the other spin orientation. Therefore, HMM materials are conductors for one spin channel (usually the majority one) and insulators for the other spin channel (usually the minority one) leading to a full spin polarization at the Fermi energy. This remarkable property was predicted in 1983 by de Groot [1] in the half-Heusler  $\text{NiMnSb}$  compound. Since this pioneering theoretical work, other full-Heusler compounds were predicted to host this band-structure behavior (see, for instance, Ref. [2]). A pivotal step was reached after the robust HMM experimental confirmation (by using

\*stephane.andrieu@univ-lorraine.fr

†Present address: CINAM, Aix-Marseille Université, Marseille 13009, France.

‡Present address: ICMN, Université d'Orléans/CNRS, Orléans 45071, France.

spin-resolved photoemission spectroscopy) in the full-Heusler  $\text{Co}_2\text{MnSi}$  compound [3,4]. This HMM behavior was thus explored in other  $\text{Co}_2\text{Mn}$ -based Heusler compounds [5]. Even more interesting, high spin polarization and low magnetic damping are linked together [6]. Indeed, due to the lack of density of states for one spin channel at the Fermi energy in HMM, the spin relaxation by spin-flip mechanism is prohibited. It is then obvious that these compounds are predicted to host low magnetic damping. We reported magnetic damping coefficients as low as  $4 \times 10^{-4}$  and  $5.5 \times 10^{-4}$  in  $\text{Co}_2\text{MnSi}$  and  $\text{Co}_2\text{MnGe}$ , respectively [5], which are the lowest values obtained on conducting thin films up to now. This analysis finally highlighted that  $\text{Co}_2\text{MnSi}$  and  $\text{Co}_2\text{MnGe}$  are excellent candidates for alternative spintronic devices.

One of the remaining challenges for  $\text{Co}_2\text{MnZ}$  compounds is the achievement of PMA. Indeed, in thin-film geometry, the demagnetizing field forces the magnetization to be in plane. Nevertheless, it is possible to overcome the shape anisotropy by playing on magnetocrystalline anisotropy in bulk or generated at the surfaces and interfaces. The main problem is that  $\text{Co}_2\text{MnZ}$  compounds have low magnetocrystalline anisotropy. Thankfully, other Heusler alloys host strong magnetocrystalline anisotropy that allows the demagnetizing field to be overcome and the PMA to be obtained. These alloys belong to the  $\text{Mn}_3\text{Z}$  family [7] and have attracted a lot of attention. When the growth is realized in the  $\text{D0}_{22}$  structure, the unit cell has a tetragonalized shape and is elongated along its  $c$  axis with a  $c/a$  ratio of the order of 1.8. Such a unit cell allows an easy magnetization axis to be obtained along the  $c$  direction. It is therefore possible by choosing carefully the substrate or the buffer layer to complete the growth along this peculiar axis and obtain PMA. The growing interest on material with strong bulk magnetic anisotropy has led to several density-functional calculations on various Mn-based Heusler alloys [7–11]. A lot of  $\text{Mn}_3\text{Z}$  alloys have been identified to potentially grow in distorted phases but only a few of them have been reported experimentally, namely  $\text{Mn}_3\text{Ga}$  [12–18],  $\text{Mn}_3\text{Ge}$  [9,19–25], and  $\text{Mn}_3\text{Sn}$  [26]. It appears that the most attractive tetragonal compounds are  $\text{Mn}_3\text{Ga}$  and  $\text{Mn}_3\text{Ge}$  since they host, for instance, high PMA, high Curie temperature or low saturation magnetization. Finally, some experimental works have been published using  $\text{Mn}_{100-x}\text{Z}_x$  layers, essentially with  $Z = \text{Ge}$  and  $\text{Ga}$ . A detailed review is given in the first part of this paper. Even if PMA is often observed, the reported magnetic properties are very different from one paper to the other. Stoichiometry and chemical ordering turn out to be very useful to keep the interesting properties. However, extracting clear trends from the existing literature proves to be challenging.

In this paper, we propose to investigate in detail the PMA in these alloys and compounds thanks to our molecular beam epitaxy (MBE) setup that allows us to control

the stoichiometry of binary, ternary, or quaternary alloys with an accuracy close to 1% [27]. Moreover, the possibility to heat the layers during and/or after the growth allows us to obtain an optimized chemical ordering. A first step of this study was to characterize the structural and magnetic properties of  $\text{Mn}_{100-x}\text{Ga}_x$  and  $\text{Mn}_{100-x}\text{Ge}_x$  thin films by varying  $x$  from 0 to 100 in order to choose the best layer combination that validates the different prerequisites for spintronic applications. The second step was to look at the replication of this PMA on the HMM layer grown on top of this buffer layer.

The films were grown by MBE. Standard structural analysis were performed *in situ* by using electron diffraction during the growth and *ex situ* by using x-ray diffraction and high-resolution transmission electron microscopy (TEM). The chemical ordering inside the unit cell was checked by using scanning TEM with high-angle angular dark-field analysis (STEM HAADF). Different magnetic characterization means were used, including magnetization measurement [superconducting quantum interference device vibrating sample magnetometer (SQUID VSM) and/or physical property measurement system vibrating sample magnetometer (PPMS VSM)], sensitive to the whole sample, including the substrate, x-ray magnetic circular dichroism (XMCD), interesting because of its element-specific sensitivity, and *in situ* magneto-optical Kerr effect (MOKE) to probe the top film without interference from the substrate. The paper is organized into seven sections. The second section is dedicated to a review of published works on thin films made of Mn-Ga and Mn-Ge alloys. Growth details and characterization means used in this study are presented in the third section. The fourth section focused on PMA in  $\text{Mn}_{100-x}\text{Ga}_x$  and  $\text{Mn}_{100-x}\text{Ge}_x$  thin films alone. The fifth section is dedicated to the replication of this PMA in a HMM material using XMCD to get information from both  $\text{Mn}_3\text{Ge}$  and HMM layers separately. As Mn is present in both layers using  $\text{Co}_2\text{Mn}$ -based HMM films,  $\text{Co}_2\text{FeGe}$  films grown on  $\text{Mn}_3\text{Ge}$  were thus preferred for such XMCD measurements. In the sixth section, we focused on the PMA replication in the most interesting  $\text{Co}_2\text{Mn}$ -based HMM, i.e.,  $\text{Co}_2\text{MnSi}$  and  $\text{Co}_2\text{MnGe}$ , by using a dedicated UHV MOKE setup. The samples were thus measured just after the growth all under UHV. Note that we also studied in this section the  $\text{Mn}_3\text{Ge}/\text{Co}_2\text{FeGe}$  already fully characterized by XMCD in the previous section. Finally, all the results are summarized and compared to the literature in the last section.

## II. LITERATURE REVIEW ON $\text{Mn}_3\text{Z}$ AND STRATEGY OF THE PRESENT WORK

### A. $\text{Mn}_3\text{Z}$ compounds in general

While the big majority of Heusler alloys are cubic leading to zero PMA, some of them can crystallize in distorted structures that may host strong PMA. Such distortions are

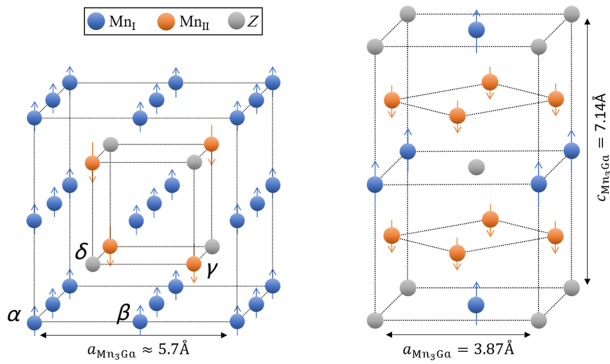


FIG. 1.  $D0_3$  cubic structure on the left and  $D0_{22}$  tetragonal structure on the right of  $Mn_3Z$  compounds. In the  $D0_{22}$  structure,  $Z$ ,  $Mn_I$ , and  $Mn_{II}$  are, respectively, in Wyckoff positions  $2a \rightarrow (0, 0, 0)$ ,  $2b \rightarrow (\frac{1}{2}, \frac{1}{2}, 0)$ , and  $4d \rightarrow (\frac{1}{2}, 0, \frac{1}{4}), (0, \frac{1}{2}, \frac{1}{4})$ .

predicted to potentially host huge bulk magnetocrystalline anisotropy coefficient  $K_V$ , especially in Mn-based Heusler alloys ( $Mn_3Z$  family). Different structures for  $Mn_3Z$  alloys have been identified in the literature with the most popular ones being the cubic  $D0_3$  structure, the hexagonal  $D0_{19}$  structure, and the tetragonal  $D0_{22}$  structure. Two of them are represented in Fig. 1. As one can see, full-Heusler compounds contain two different magnetic sublattices coming from the different chemical environments felt by atoms in both sublattices. This can lead to peculiar spin arrangement as, for instance, ferromagnetism, antiferromagnetism, or ferrimagnetism.

The  $D0_3$  structure is a classical cubic structure. Usually,  $D0_3$  phase is used to point out disorder between  $X$  and  $Y$  atoms in the  $X_2YZ$  Heusler unit cell. Here, since  $X$  and  $Y$  atoms are Mn atoms,  $D0_3$  structure corresponds to an ordered structure and this nomenclature is only due to the presence of Mn in three crystallographic sites. The studies performed on  $D0_3$   $Mn_3Z$  compounds aim to get half-metal-compensated ferrimagnets. The  $D0_3$  structure is predicted to possibly generate a moment compensation of Mn atoms on their different crystallographic sites. In 2006, Wurmehl *et al.* [28] predicted a half-metallic-compensated ferrimagnetic behavior in  $D0_3$   $Mn_3Ga$ . In addition to a half-metallicity, such compounds do not have any stray field and the impact of an external magnetic field is minimized making them very promising for future applications. Unfortunately, no property of magnetocrystalline anisotropy has been determined for this structure. The hexagonal  $D0_{19}$  ( $P6_3/mmm$ , space group no. 194) structure has also been investigated for its non-collinear antiferromagnetic phase with a triangular spin configuration. This antiferromagnetic order has been predicted by first-principles density-functional theory [8] and experimentally observed in  $Mn_3Ga$  [29],  $Mn_3Ge$  [24], and  $Mn_3Sn$  [30].

The  $D0_{22}$  structure ( $I4/mmm$ , space group no. 139) is a tetragonalized version of the  $D0_3$  structure with basis vector turned by  $45^\circ$  as shown in Fig. 1. It can be viewed as a cubic phase with a distortion along the  $z$  axis that produces an easy axis for magnetic moments along this direction (i.e., along the unit cell's  $c$  axis). The growing interest on material with strong bulk magnetic anisotropy has led to several density-functional calculations on various Mn-based Heusler alloys [7–11]. A lot of  $Mn_3Z$  alloys have been identified to potentially grow in distorted phases but only a few of them have been reported experimentally, namely  $Mn_3Ga$  [12–18],  $Mn_3Ge$  [9,19–25], and  $Mn_3Sn$  [26] since the stabilization of tetragonal phase can be complex as explained by Zhang *et al.* [8] for  $Mn_3Sn$ . Moreover, chemical ordering turns out to be very useful to keep the interesting properties. The most attractive tetragonal compounds are  $Mn_3Ga$  and  $Mn_3Ge$  since they are ferrimagnetic in bulk and host high PMA, high Curie temperature, or low saturation magnetization.

## B. $Mn_3Ga$ compound and $Mn_{100-x}Ga_x$ alloys

As said before, density-functional calculations [7,8,10,11] have been performed on  $Mn_3Ga$  compound to unveil its outstanding properties. Its experimental study has begun in 1970 with the work of Kren *et al.* [12] who investigated the growth of  $Mn_{2.85}Ga_{1.15}$ . First of all, they obtained the hexagonal  $D0_{19}$  phase with a weak ferromagnetic behavior. An annealing up to 750 K leads to the tetragonal  $D0_{22}$  Heusler structure with a  $c/a$  ratio of 1.824. Thanks to neutron diffraction, they measured a ferrimagnetic order coming from the two nonequivalent Mn sites, which results in a  $Mn_I$  moment of  $-2.8 \pm 0.2\mu_B$  and a  $Mn_{II}$  moment of  $1.6 \pm 0.2\mu_B$ . As the  $D0_{22}$  structure is made of two inequivalent Mn crystallographic sites with  $Mn_I$  and  $Mn_{II}$ , respectively, in Wyckoff position  $2b$  and  $4d$ , the Ga atom is in  $2a$  position. The Mn in  $2b$  and  $4d$  positions are coupled antiferromagnetically resulting in an overall ferrimagnetic structure as sketched in Fig. 1. The alternating planes of up and down moments are expected to be collinear and aligned along the  $z$  direction.

Many years later, Balke *et al.* [13] showed with theoretical calculations and experiments that the  $D0_{22}$  phase presents a ferrimagnetic order coming from partially compensated moments in accordance with previous works. Moreover, they found theoretical moments on  $Mn_I$  and  $Mn_{II}$  sites of, respectively,  $-2.896\mu_B$  and  $2.355\mu_B$ , which give rise to a total moment of  $M_{tot} = 1.77\mu_B$ . Thanks to electronic structure calculations, they predicted a nearly half-metallic ferrimagnet with 88% of spin polarization at the Fermi energy and experimental results gave a Curie temperature of 762 K. Finally, they showed moment tunability from 0 to  $1\mu_B$  by changing the Mn ratio from  $Mn_3Ga$  to  $Mn_{2.85}Ga$ . The work of Balke *et al.* was confirmed by the publication of Winterlik *et al.* [14], which

goes further. They studied  $\text{Mn}_{3-x}\text{Ga}$  with  $x$  varying from 0 to 1. Every compound crystallized in the  $\text{D0}_{22}$  structure. Furthermore, volume and  $c/a$  ratio increased with Mn contents while moments decreased from  $0.47\mu_B$  to  $0.26\mu_B$  and were lower than the theoretical values determined by Balke *et al.* [13]. Both works showed a high magnetocrystalline anisotropy when  $\text{Mn}_3\text{Ga}$  grows in the  $\text{D0}_{22}$  Heusler phase. This property comes from the highly tetragonal structure with a  $c/a$  ratio around 1.8 [12–14] leading to  $K_V$  values of the order of 1 to 3  $\text{MJ m}^{-3}$  [31,32].

The collinear arrangements between the two Mn sublattices are still under debate. In 2013, Rode *et al.* [16] published a paper focusing on the magnetic moments and especially the magnetic structure of tetragonal  $\text{D0}_{22}$   $\text{Mn}_3\text{Ga}$ . They labeled the origin of the strong magnetic anisotropy to the Mn  $4d$  site and observed for some samples a soft intrinsic in-plane component resulting in a noncollinear structure and coming from the Mn  $2b$  site. This noncollinear structure is explained by the  $2b$ -site in-plane anisotropy and by the competing Mn-Mn interactions. Nowadays, the exact magnetic structure of  $\text{Mn}_3\text{Ga}$  is still unclear. Substrates and buffer layers play a role on thin-film constrain together with chemical ordering lying in the sample, which are probably of primary interest to explain the different results reported in the literature.

Despite this complex magnetic behavior, many papers have reported the growth of  $\text{D0}_{22}$   $\text{Mn}_3\text{Ga}$  on numerous substrates or buffer layers such as  $\text{MgO}$  [15–17],  $\text{SrTiO}_3$  [16],  $\text{GaAs}$  [18],  $\text{Pt}$  [15],  $\text{Cr}$  [15,31,32]. All of them state the presence of a tetragonalized structure with a  $c/a$  ratio of the order of 1.8. All the samples present an easy axis of magnetization out of plane with a strong uniaxial magnetocrystalline anisotropy always estimated close to  $\text{MJ m}^{-3}$ . Typical values for magnetocrystalline anisotropy and saturation magnetization are as follows:  $K_V \approx 1$  to  $1.5 \text{ MJ m}^{-3}$ ,  $M_s \approx 200$  to  $600 \text{ emu cm}^{-3}$  depending on alloy stoichiometry. Hysteresis loops performed on  $\text{Mn}_3\text{Ga}$  do not present a perfectly squared shape but a strong perpendicular easy axis is always observed. This strong easy axis in magnetization results in difficulties to reach saturation with an in-plane applied magnetic field [18,25].

### C. $\text{Mn}_3\text{Ge}$ compound and $\text{Mn}_{100-x}\text{Ge}_x$ alloys

Similarly to Mn-Ga, Mn-Ge binary compounds possess a manifold of stable phases [33] but only the  $\text{sD0}_{22}$  structure is of interest here.  $\text{D0}_{22}$   $\text{Mn}_3\text{Ge}$  is isomorphic to  $\text{D0}_{22}$   $\text{Mn}_3\text{Ga}$  but has been less investigated despite similar properties. The first reported paper on the tetragonal version of  $\text{Mn}_3\text{Ge}$  dates back to 1961 [34] and the first magnetic study was performed by Krén *et al.* [35] in 1971 unveiling the presence of the two different Mn moments with, respectively,  $\text{Mn}_I = -2.8 \pm 0.3\mu_B$  and  $\text{Mn}_{II} = 1.6 \pm 0.2\mu_B$ , respectively. The structure is organized similarly to  $\text{Mn}_3\text{Ga}$  leading to a ferrimagnetic

behavior. Studies done to make use of the strong magnetocrystalline anisotropy of  $\text{D0}_{22}\text{Mn}_3\text{Ge}$  arrived during the 2010s [8,9,19,20,22,23,25,36]. The group of Kurt [9] investigated tetragonal  $\text{Mn}_3\text{Ge}$  for its potential applications on nanoscale spin valve or magnetic tunnel junction (MTJ). They mastered  $\text{Mn}_3\text{Ge}$  growth on  $\text{SrTiO}_3$  substrate with a  $c/a$  ratio of 1.866 in accordance with the  $\text{D0}_{22}$  structure. Magnetization measurement confirms the out-of-plane easy magnetization axis with a huge coercivity  $\mu_0 H_C = 2.3 \text{ T}$  and a resulting anisotropy constant  $K_u = 0.91 \text{ MJ m}^{-3}$ . Magnetic measurement with the field applied parallel to the surface unveils a small in-plane component that may be a consequence of frustration of some of the exchange bonds. They measured the spin polarization at the Fermi level by point-contact Andreev reflection with a resulting value of 46% well below the theoretical value of 75% obtained by density-functional calculations. After this investigation, other groups tried to control the  $\text{D0}_{22}$   $\text{Mn}_3\text{Ge}$  growth on various types of substrate or buffer layers such as  $\text{MgO}$  [36],  $\text{Cr}$  [19,20,22,25], or  $\text{Ru}$  [23] studying particularly stoichiometric and off-stoichiometric  $\text{Mn}_{3-x}\text{Ge}$  alloys to investigate the robustness of the  $\text{D0}_{22}$  phase and the impact of stoichiometry on the relevant properties [19,20,36]. The most relevant effect for STT and SOT applications revealed by Ref. [19] is the nonsquare shape obtained for off-stoichiometry samples. It must be noted that nonsquare shapes are also obtained for stoichiometric  $\text{Mn}_3\text{Ge}$  samples grown on  $\text{SrTiO}_3$  [9],  $\text{MgO}$  [36], and  $\text{Ru}$  [23] seed layer. Nonetheless, magnetocrystalline anisotropy  $K_u$ , saturation magnetization  $M_s$  and  $c/a$  ratio stay in the same range. As a summary, the main experimental properties values extracted from the literature [8,9,19,20,22,23,25,36] for stoichiometric  $\text{D0}_{22}$   $\text{Mn}_3\text{Ge}$  are as follows:  $K_u \approx 2 \text{ MJ m}^{-3}$ ,  $M_s \approx 100 \text{ emu cm}^{-3}$ ,  $P = 46\%$ , and a  $T_C$  above 800 K. Theoretical papers attest to the good properties of  $\text{Mn}_3\text{Ge}$  [7,9,11,36]. Theoretical  $K_u$ ,  $M_s$ , and  $P$  values are always higher than the experimental ones. For instance, Mizukami *et al.* [36] calculated an anisotropy value of  $K_u = 2.3 \text{ MJ m}^{-3}$ , a net magnetization of  $M_s = 180 \text{ emu cm}^{-3}$  and a spin polarization at the Fermi energy of  $P = 77\%$ . The mismatch between theory and experience is not yet fully understood but off-stoichiometry and chemical order may influence these properties. Moreover, they predicted a low damping value of  $\alpha = 9 \times 10^{-4}$  with an identified fully spin-polarized  $\Delta_1$  band at the Fermi level that makes  $\text{Mn}_3\text{Ge}$  even more promising than  $\text{Mn}_3\text{Ga}$  as MTJ electrodes with a tunneling barrier, such as  $\text{MgO}$ .

### D. $\text{Mn}_3\text{Z}/\text{Co}_2\text{YZ}'$ bilayers and superlattices

Preliminary results on MTJ or SOT effect using  $\text{Mn}_3\text{Ga}$  have been published over the years [18,25,37] but our attention focuses on  $\text{Mn}_3\text{Z}/\text{Co}_2\text{YZ}'$  compounds here. Only two groups published papers dealing with the growth of such Heusler compounds' bilayers or superlattices

(SLs). The group of Mizukami at Tohoku University published several papers on Heusler bilayers grown by UHV sputtering. They grew  $D0_{22}$   $Mn_3Ga/Co_2FeAl$  [38–41],  $Co_2FeSi$  [39–41],  $Co_2MnSi$  [40–42],  $Co_2MnAl$  [40,41] and managed to obtain out-of-plane magnetized bilayers with a perfect growth of Mn-Ga alloys along its  $c$  axis. At least different magnetic behaviors were reported from one system to the other. On the one hand, this group prepared Mn-Ga-based stacks with small Mn-Ga thicknesses (1 to 6 nm). They reported square loops in  $Mn_{62}Ga_{38}/Co_2FeAl(0.5\text{--}2\text{ nm})$  superlattices annealed at  $400^\circ\text{C}$  [38] and analyzed their results by considering some antiferromagnetic coupling between Mn-Ga and  $Co_2FeAl$ . Almost at the same time, they reported either ferromagnetic or antiferromagnetic coupling on the same system depending on the annealing temperature [39]. On the other hand, the same group studied several full Heuslers films grown on 30-nm-thick  $Mn_{70}Ga_{30}$  also annealed at  $400^\circ\text{C}$  after the growth [40]. They reported hysteresis loops with a two-step switching explained by an antiferromagnetic exchange coupling at the  $Mn_{70}Ga_{30}$  interface with  $Co_2FeAl$ ,  $Co_2MnAl$ ,  $Co_2FeSi$ , and  $Co_2MnSi$  based on VSM and MOKE measurements. One should note that the loop shapes observed by MOKE are intriguing and explained by considering limited depth of MOKE analysis. We will see in this study a trivial explanation of this effect.

Another group reported similar behavior for  $Mn_3Ga/Co_2MnSi$  heterostructures prepared by molecular beam epitaxy [43]. In this study, 30-nm-thick Mn-Ga layers were grown. Since the epitaxy of MgO on top of a  $Mn_3Ga$  film is of bad quality probably because of the large misfit, they built  $Mn_3Ga$ -based perpendicular-MTJ with the help of  $Co_2MnSi$  alloy. The  $Mn_{3.1}Ga/Co_2MnSi/MgO/Co_2MnSi/Mn_{2.9}Ga$  structure was investigated and a strong antiferromagnetic coupling is observed. To summarize, the magnetic coupling between Mn-Ga or Mn-Ge and  $Co_2YZ'$  full Heuslers seems to strongly depend on the bilayer characteristics and preparation. Factors such as the Mn-Z stoichiometry and thickness, the choice and thickness of  $Co_2YZ'$ , and the annealing process (or lack thereof) may significantly influence the magnetic coupling behavior.

### III. EXPERIMENTAL DETAILS

This review clearly shows that very different magnetic properties were reported for systems that seem to be close or identical. Hysteresis loops with two-step switching were sometimes observed, sometimes not, without any clear explanation. Moreover, the alloy stoichiometry is often not the same in published papers, leading to different hysteresis loop shape or different interfacial exchange coupling values. Our MBE facility is of particular interest to better understand these magnetic properties since we are able

to control the stoichiometry with an accuracy around 1% [27]. The first step of our study was thus to vary the stoichiometry by growing  $Mn_{100-x}Ga_x$  and  $Mn_{100-x}Ge_x$  alloys. This allowed us to study the structural and magnetic behavior of these films for perfect chemical ordering like in  $Mn_3Z$  ( $x = 25$ ) but also for off stoichiometric compositions. The second step was to grow HMM  $Co_2MnSi$  or  $Co_2MnGe$  on top of these buffer layers and to maintain PMA in the whole stack.

All the films were grown and characterized using the Daum tube facility at Jean Lamour Institute. This 70-m-long UHV tube is equipped with 30 machines. Three setups were used in this study: the quaternary MBE, equipped with three e-guns with six pockets each and six Knudsen cells (24 available materials), a standard Auger/x-ray spectroscopy facility for chemical analysis, and a UHV MOKE system in polar geometry to measure the hysteresis loops along the growth direction (Fig. S1 within the Supplemental Material [44]).  $MgO(001)$  substrates were used since many metallic films can be epitaxially grown on top of it (see, for instance, Ref. [45]).  $MgO$  substrate was outgassed *in situ* at a temperature around  $700^\circ\text{C}$  (measured with a pyrometer focused on the sample surface using an arbitrary chosen emissivity equal to 0.85 for all the films) to clean the surface. Straight after, a 10-nm-thick  $MgO$  layer was deposited around  $650^\circ\text{C}$  to bury the residual carbon contamination and smooth the surface.

Since  $Mn_3Z$  growth attempts on  $MgO$  substrate were not successful [11], three different buffer layers were therefore tested:  $Pd(001)$ ,  $V(001)$ , and  $Cr(001)$ . A V-buffer layer was tested due to its resistance to intermixing with many elements up to quite large substrate temperatures. However, it was rapidly disqualified because  $Mn_3Ga$  grows on it in its  $D0_3$  cubic structure [46]. In contrast, the  $D0_{22}$  phase was already obtained using Pd- and  $Cr(001)$ -buffer layers [13, 15, 19, 20, 22, 25, 32, 46]. In theory a Pd-buffer layer is ideal since its cell parameter [fcc –  $a_{Pd}(001) = 3.89\text{ \AA}$ ] fits perfectly to in-plane  $Mn_3Ga$  one. Cr is also a good candidate [bcc –  $2a_{Cr}(011) = 4.07\text{ \AA}$ ]. The Pd(Cr)/ $Mn_3Z$  layers' intermixing temperature dependence was studied using Auger spectroscopy and no intermixing was observed up to  $400^\circ\text{C}$ . However, we limited the growth temperature of HMM  $Co_2MnSi$  or  $Co_2MnGe$  on top of  $Mn_3Z$  layers to  $250^\circ\text{C}$  since intermixing between the layers was observed to start around  $300^\circ\text{C}$ . The second step was thus to check the replication of  $Mn_3Z$  PMA on the Heusler HMM compounds grown on top. This goal was however constrained by many experimental limits. First, the basic  $Mn_3Z/X_2YZ'$  block useful for XMCD eliminates the choice of  $Co_2MnZ'$  compounds since Mn is in both layers. We consequently choose the  $Mn_3Z/Co_2FeGe$  block for XMCD studies. Second, if a  $Mn_3Z/Co_2FeGe$  bilayer is pertinent for XMCD studies, the amount of materials is too small for VSM and MOKE measurements. Superlattices (with five repetitions)

were thus grown for these former techniques. All these constraints lead to the following samples:

(a)  $\text{Mn}_{100-x}\text{Ga}_x$  and  $\text{Mn}_{100-x}\text{Ge}_x$  thin films grown on Pd- or Cr-buffer layers, analyzed by VSM and XMCD (Sec. IV).

(b)  $\text{Mn}_3\text{Ge}/\text{Co}_2\text{FeGe}$  bilayers especially dedicated for XMCD (Sec. V).

(c)  $\text{Mn}_3\text{Ge}/\text{Co}_2\text{FeGe}$  superlattices to test MOKE measurements (comparing to XMCD) (Sec. VI).

(d)  $\text{Mn}_3\text{Ga}/\text{Co}_2\text{MnSi}$ ,  $\text{Mn}_3\text{Ge}/\text{Co}_2\text{MnGe}$ , and  $\text{Mn}_3\text{Ge}/\text{Co}_2\text{MnSi}$  bilayers or superlattices for MOKE measurements (Sec. VI).

The SQUID VSM and PPMS VSM measurements were performed on standard commercial setups. The MOKE measurements were performed on the UHV MOKE chamber connected to the IJL Daum tube (Fig. S1 within the Supplemental Material [44]). The XMCD measurements were performed at the Boreas beamline of the ALBA synchrotron under a UHV environment. Boreas beamline is equipped with superconducting coils allowing application of magnetic field up to 6 T along the beam. A cryostat enables ultralow temperature studies (4 to 350 K) and a full polarization control is possible on an extended soft x-ray range going from 80 to 4000 eV.

## IV. PMA IN $\text{Mn}_{100-x}\text{Z}_x$ FILMS ( $Z = \text{Ga}, \text{Ge}$ )

### A. $\text{Mn}_{100-x}\text{Ga}_x$ films

50-nm-thick Mn-Ga layers were deposited on a 10-nm-thick Pd-buffer layer. Mn and Ga were evaporated using Knudsen cells with fluxes fixed to  $\Phi_{\text{Mn}} + \Phi_{\text{Ga}} = 2 \times 10^{14}$  at/cm<sup>2</sup>/s and  $(100 - x)\Phi_{\text{Ga}} = x\Phi_{\text{Mn}}$ . The Mn-Ga films were grown around 250 °C to avoid intermixing with Pd, as checked by Auger spectroscopy. The epitaxial process was checked using reflection high-energy electron diffraction (RHEED). The RHEED patterns are given in Fig. 2 and confirm the expected epitaxial relationship as  $\text{Mn}_{100-x}\text{Ga}_x$  [100](001)//Pd [100](001)//MgO [100](001). Such RHEED patterns indicate a nice epitaxy with flat surfaces. It should be noted that half streaks appear along Mn-Ga [110] azimuth for  $x = 25$  ( $\text{Mn}_3\text{Ga}$ ) and persist for  $x = 20$  and 15%. These half streaks are a proof that chemical ordering took place (similar to  $\text{Co}_2\text{MnZ}'$  epitaxy, see Ref. [27]). Although the first interest of RHEED is to check the epitaxial process during the growth, it is also a very accurate technique to test the atomic fluxes and thus the final stoichiometry. Indeed, RHEED intensity oscillations are generally observed in the case of a two-dimensional growth process (meaning that the film grows layer by layer). The delay to complete one (or two) atomic layers is thus completely fixed by the fluxes. As the fluxes were firstly calibrated using a quartz microbalance, the delay to

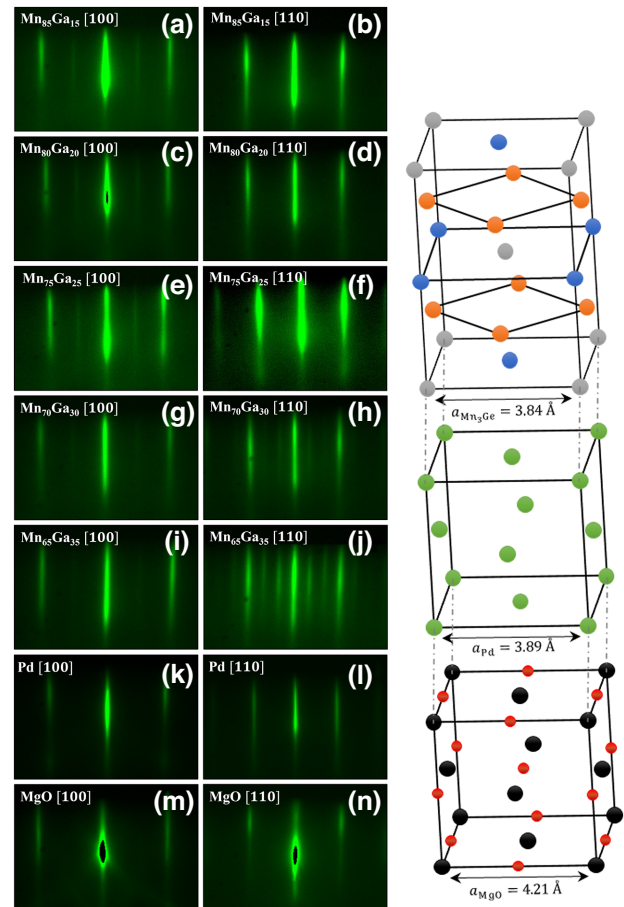


FIG. 2. RHEED patterns with the electron beam applied along the [100]<sub>MgO</sub> and [110]<sub>MgO</sub> azimuths for  $\text{Mn}_{85}\text{Ga}_{15}$  (a),(b),  $\text{Mn}_{80}\text{Ga}_{20}$  (c),(d),  $\text{Mn}_{75}\text{Ga}_{25}$  (e),(f),  $\text{Mn}_{70}\text{Ga}_{30}$  (g),(h),  $\text{Mn}_{65}\text{Ga}_{35}$  (i),(j), the Pd-buffer layer (after annealing) (k),(l), the MgO substrate (m),(n). On the right, sketch of the epitaxial relationships between the layers.

complete a layer is thus calculated and afterwards compared to the period measured on RHEED oscillations. We systematically use this method to check the stoichiometry [27] (but a 2D growth is needed). For example, for  $x = 25\%$  ( $\text{Mn}_3\text{Ga}$ ), the time to complete a layer extracted from our calibrated fluxes is equal to  $6.68 \pm 0.1$  s to compare to RHEED oscillations' period equal to  $6.7 \pm 0.1$  s (Fig. S2 within the Supplemental Material). Another proof of the good control of the fluxes is obtained from low-angle x-ray reflectivity that gives the thickness of a thin film. Again, the target thicknesses of the films (50 nm) were confirmed by x-ray reflectivity with an accuracy around 1% (Fig. S2 within the Supplemental Material). All these results allow us to confirm the accuracy on the stoichiometry around 1% for Mn-Ga alloys.

As RHEED gives only information on the surface lattice, regular x-ray diffraction experiments were performed in the  $\theta/2\theta$  mode for the whole series after capping with

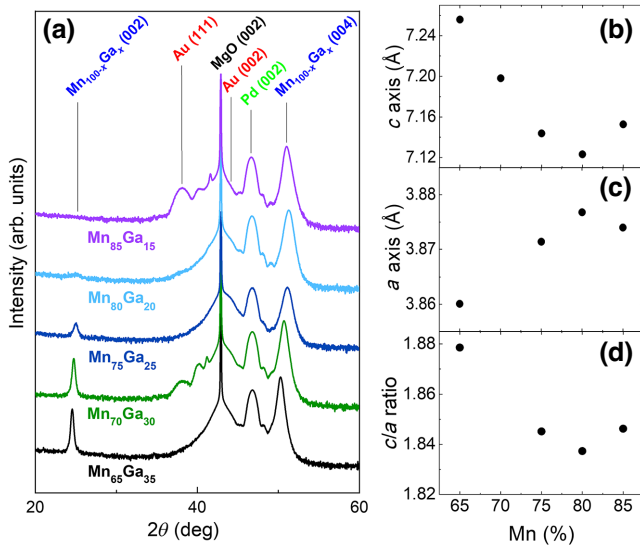


FIG. 3. (a)  $\theta/2\theta$  x-ray diffraction spectra of the  $\text{Mn}_{100-x}\text{Ga}_x$  series with  $x = 15, 20, 25, 30,$  and  $35$ . (b)  $c$  parameter extracted from the (004) peaks. (c)  $a$  parameter extracted from nonspecular measurements. (d) Resulting  $c/a$  ratio.

a 5-nm-thick gold layer. The results are shown in Fig. 3. The extracted cell parameter gives an out-of-plane parameter  $c$  varying from 7.13 to 7.26 Å. In addition, the in-plane lattice parameters were extracted by looking at (204) diffraction peaks (not shown) and stand very closely to the Pd-buffer layer one. The  $c/a$  ratio are then calculated. All these values plotted in Figs. 3(b)–3(d) are in perfect agreement with the  $\text{D}_{022}$  phase observed in the literature [13,17,18]. Some information on the chemical ordering can also be extracted from this analysis. Indeed, the peaks' intensity in the case of this  $\text{D}_{022}$  cell with a perfect chemical ordering leads to higher intensities for  $h + k + l = 4n$  peaks compared to  $h + k + l = 4n + 2$  ones. If a random chemical disorder occurs in the cell, the  $h + k + l = 4n + 2$  peak vanishes. This contribution is clearly visible for  $x = 25, 20,$  and  $15\%$  meaning that chemical ordering took place. If x-ray diffraction may be used to determine the chemical ordering in the cell, we have shown that this is not obvious in  $\text{Co}_2\text{MnZ}'$  compounds [27], and should be even harder in  $\text{Mn}_2\text{MnZ}$  compounds. We use STEM for this task as will be seen hereafter. Finally, note that the Au capping was observed to grow along the (111) or/and (001) crystalline directions depending on the misfit as already observed on several  $\text{Co}_2\text{MnZ}'$  compounds [27]. The (002) resulting peak is hardly distinguishable on the XRD spectra due to its broadness (low thickness) and proximity with (002) MgO and (002) Pd peaks.

The magnetic properties of the  $\text{Mn}_{100-x}\text{Ga}_x$  series were studied using vibrating sample magnetometry performed at room temperature applying the field out of plane of the sample. As the entire sample was probed, the diamagnetic

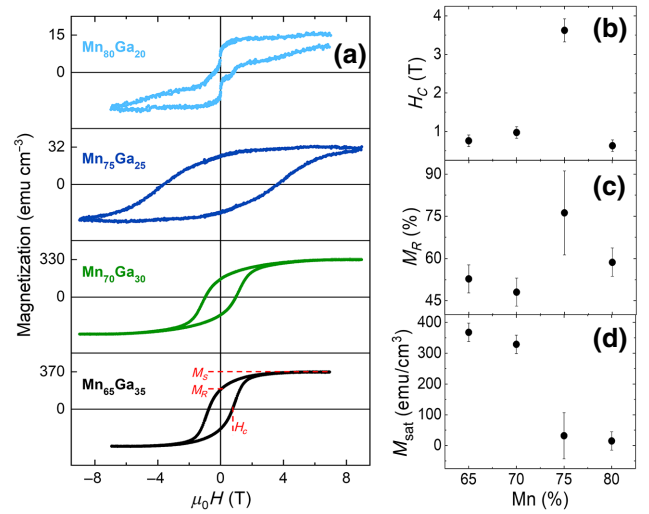


FIG. 4. (a) Hysteresis loops measured using a PPMS VSM with an out-of-plane applied magnetic field for the  $\text{Mn}_{100-x}\text{Ga}_x$  series with  $x = 20, 25, 30,$  and  $35$ . (b)–(d) are, respectively, the coercive field, the remanence, and the saturation magnetization.

contribution (slope correction) coming from MgO was subtracted to get the layer hysteresis loops as shown in Fig. 4. In-plane measurements were also performed but not shown here since saturation was never reached even at 7 T. Indeed, it was thus very difficult to correctly subtract the diamagnetic contribution from MgO and hence to get the correct signal coming from the layer. One can see in Fig. 4 that each composition shows a clear cycle opening in the out-of-plane direction as a result of PMA, except for  $x = 15\%$  (not shown) for which we observed only the diamagnetic MgO contribution (meaning negligible magnetization for the  $\text{Mn}_{85}\text{Ga}_{15}$  layer). For the other concentrations, the hysteresis loops do not exhibit a square shape and are bent as seen in the literature. This analysis leads us to key conclusions:

- (i) For large Mn concentration ( $x < 20\%$ ), very small magnetizations (or even zero) are detected, which can be explained by the tendency of the alloys to be antiferromagnetic (as in pure Mn).
- (ii) For  $x = 25\%$ , the magnetization is still small, a huge magnetocrystalline anisotropy is present, and the magnetization reversal operates from 0 to 8 T. These observations are in agreement with a ferrimagnetic behavior.
- (iii) For higher Ga concentrations, the PMA anisotropy is decreasing but still there, and the magnetic moment strongly increases.
- (iv) The magnetization at remanence does not exceed 80%.

To summarize, we confirm, on the one hand, the large magnetocrystalline anisotropy in  $\text{D}_{022}$  Mn-Ga-based alloys but we show here that the resulting PMA parameters



(such as remanent magnetization and coercive field) are strongly dependent on the stoichiometry. On the other hand, the nonsquareness of the loops with uncomplete remanent magnetization are not the ideal magnetic behaviors needed for spintronic devices. Nonetheless, these behavior may be affected when growing  $\text{Co}_2\text{MnSi}$  or  $\text{Co}_2\text{MnGe}$  on top of it.

### B. $\text{Mn}_{100-x}\text{Ge}_x$ films

A similar study was performed on 50-nm-thick Mn-Ge layers first grown on Pd-buffer layers. Similar fluxes and substrate temperatures were used. The resulting RHEED patterns are given in Fig. 5 for the whole  $\text{Mn}_{100-x}\text{Ge}_x$  series. In contrast to Mn-Ga alloys, two epitaxial regimes were observed depending on the Mn-Ge concentrations. For  $x < 25\%$ , RHEED patterns are typical of the  $\text{D0}_{22}$  structure. Nonetheless, the epitaxial process completely changes for higher Ge concentration. This observation is not surprising since other compounds, such as  $\text{Mn}_5\text{Ge}_3$

( $x = 37.5$ ) or  $\text{Mn}_2\text{Ge}$  ( $x = 33$ ) are stable [33]. The stoichiometry was again checked using RHEED intensity oscillations and low-angle x-ray diffraction (Fig. S2 within the Supplemental Material). The main difference with Mn-Ga alloys is that the bilayer-by-bilayer growth mode is observed at least for the  $\text{Mn}_3\text{Ge}$  compounds, which is a strong indication of a perfect chemical ordering [27] in this case.

XRD measurements are plotted in Fig. 6 for the  $\text{Mn}_{100-x}\text{Ge}_x$  series. Two types of diagrams were obtained: similar to Mn-Ga ones for  $x = 15, 20, 25$  and corresponding to the  $\text{D0}_{22}$  structure, but different for  $x = 30$  and 33 where additional diffraction peaks corresponding to another phase are visible. These unknown peaks are indexed with black diamonds in the curve of  $\text{Mn}_{66}\text{Ge}_{33}$  ( $\text{Mn}_2\text{Ge}$ ). These results are in agreement with the RHEED observations. At least, this analysis shows that epitaxy is only observed for Ge concentration lower than 25% (Mn concentration higher than 75%). We thus report in Figs. 6(b)–6(d) the extracted  $a$ ,  $c$  and  $c/a$  ratio, together plotted with the values obtained in Mn-Ga alloys for comparison. The  $\text{D0}_{22}$  structures are consequently almost the same in Mn-Ga and Mn-Ge alloys, except that the in-plane parameter is lower and hence the out-of-plane  $c$  parameter bigger than in Mn-Ga. This is simply due to epitaxial strain. Similarly to  $\text{Mn}_{100-x}\text{Ga}_x$  samples, the Au capping grew along (111) or /and (001).

The magnetic properties of these Mn-Ge layers were studied using PPMS VSM measurements applying the

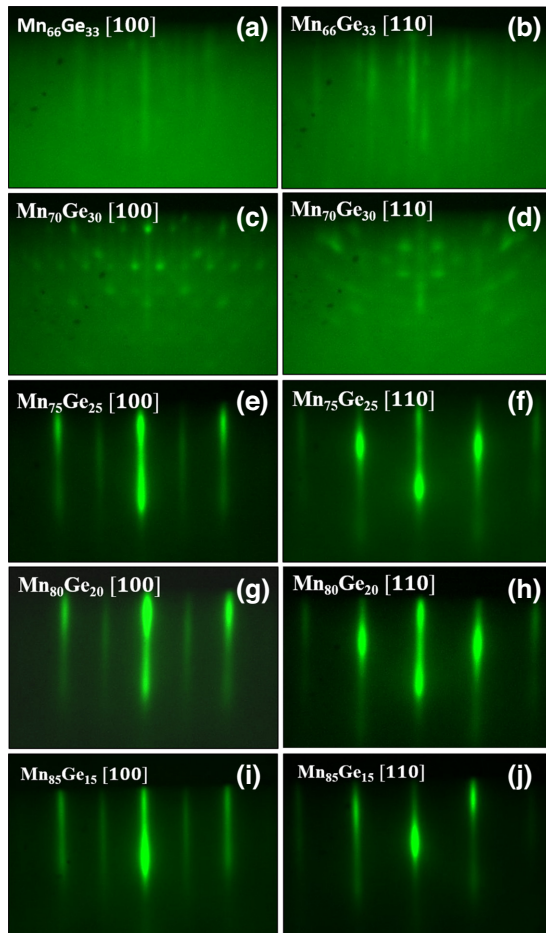


FIG. 5. RHEED patterns with a beam applied along the [100] (left) and [110] (right) MgO azimuths for  $\text{Mn}_{66}\text{Ge}_{33}$  (a),(b),  $\text{Mn}_{70}\text{Ge}_{30}$  (c),(d),  $\text{Mn}_{75}\text{Ge}_{25}$  (e),(f),  $\text{Mn}_{80}\text{Ge}_{20}$  (g),(h),  $\text{Mn}_{85}\text{Ge}_{15}$  (i),(j).

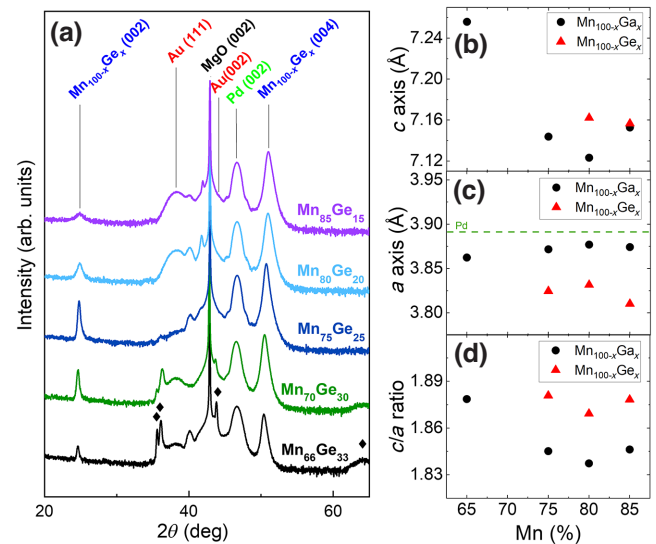


FIG. 6. (a)  $\theta/2\theta$  x-ray diffraction spectra of the  $\text{Mn}_{100-x}\text{Ge}_x$  series with  $x = 15, 20, 25, 30,$  and  $33$ . The black diamonds in  $\text{Mn}_{66}\text{Ge}_{33}$  scan identify the peaks position from other Mn-Ge phases. (b)–(d) are, respectively, the extracted  $c$ ,  $a$  and  $c/a$  parameters for the Mn-Ge  $\text{D0}_{22}$  structure, together with Mn-Ga data for comparison. The Pd in-plane lattice spacing is also indicated in (c).

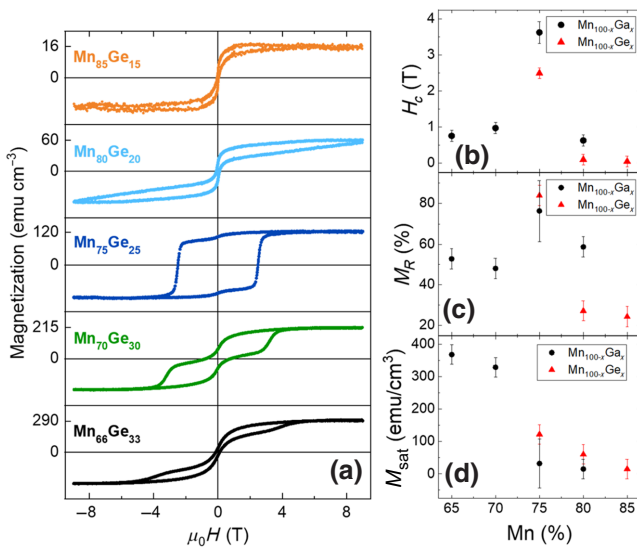


FIG. 7. (a) Hysteresis loops measured at 300 K using a PPMS VSM with out-of-plane applied magnetic field for the  $Mn_{100-x}Ge_x$  series. (b) coercive field, remanent, and saturation magnetization in both Mn-Ga and Mn-Ge films synthesized in the  $D0_{22}$  structure.

same process used for Mn-Ga alloys. The results are shown in Fig. 7. All the films show an out-of-plane easy-magnetization axis. Unlike Mn-Ga samples, the Mn-Ge alloys display a clear different hysteresis shape with regards to Mn content. For high Ge concentration, for which the Mn-Ge layers did not grow in the  $D0_{22}$  structure ( $x = 15$  and  $x = 20\%$ ), PMA is observed but two steps are clearly visible in the loops. These two steps are another proof of different phases mixing highlighted by RHEED and XRD analyses. For the three other Mn-Ge compositions where the  $D0_{22}$  structure is stable, the PMA is observed strong in  $Mn_3Ge$  but this effective anisotropy rapidly decreases when increasing the Mn content. The situation is consequently very different from Mn-Ga alloys, except for the 3:1 stoichiometry. The PMA is lower with Ge than with Ga but at least the magnetic properties of  $Mn_3Ge$  are then more appropriate for applications since squared loops, high remanence, and high coercive field were obtained. It should be noted that a double step is still observed in that case. One explanation should be due to some small areas made of another Mn-Ge phase due to a slight deviation from the perfect 3:1 stoichiometry. However, one should not forget that the entire sample (MgO + Pd + Mn – Ge layers) is probed by VSM here. As the detected magnetization is very small, any other contribution may affect the measurement. In particular, we will see in the following that this feature was never detected using XMCD and MOKE where only the top layers are probed. The next step of this study is now to look at replication of this PMA in HMM films grown on  $Mn_3Ge$ .

After this complete analysis using Pd-buffer layers, we tested the Mn-Ge growth on Cr-buffer layers also grown on MgO(001). The structural analysis (RHEED and x-ray diffraction, see Fig. S3 within the Supplemental Material [44]) showed us that the structure of  $Mn_3Ge$  films on Cr(001) is still  $D0_{22}$  with  $c = 7.12$  Å. This is a little bit smaller than on Pd buffers and is explained by a smaller misfit in  $Mn_3Ge/Pd$  than in  $Mn_3Ge/Cr$ . We actually observed that the coercive field and PMA are thus smaller, due to smaller tetragonalization. Cr layers were thus used in the following just for experimental convenience especially for our UHV MOKE setup where a maximum magnetic field of 0.9 T can be applied.

## V. PMA REPLICATION CHARACTERIZED BY XMCD

### A. $Mn_3Ge/Co_2FeGe$ bilayers on Cr(001)

$Mn_3Ge/Co_2FeGe$  bilayers were first prepared for XMCD measurements. Five samples were grown on Cr-buffer layers with a fixed 5-nm-thick  $Mn_3Ge$  and a varying  $Co_2FeGe$  thickness from 2 to 6 nm. The Au capping thickness was fixed to 2 nm for XMCD requirements. Cr and  $Mn_3Ge$  growth process is identical to the one described in the previous section. The  $Co_2FeGe$  layer is deposited on top of them and is expected to have a unit cell turned by  $45^\circ$  with respect to the above layer since  $2a_{Mn_3Ge} \approx a_{Co_2FeGe}$ . The fluxes were fixed to  $\Phi_{Co} = 2\Phi_{Fe} = 2\Phi_{Ge} = 1 \times 10^{14}$  at. cm<sup>-2</sup> s<sup>-1</sup> and the temperature deposition was set to  $250^\circ C$  to avoid interdiffusion. The RHEED and XRD experiments confirm the  $Co_2FeGe$  [110](001)// $Mn_3Ge$  [100](001)//Cr [110](001)//MgO [100](001) epitaxial relationship (Fig. S4 within the Supplemental Material). The quality of the stack was here checked by using STEM. 50–60-nm-thick cross sections were prepared along the [110] zone axis by focused ion-beam etching using Ga ions. A first chemical analysis was done on the cross section by using energy dispersive x-ray spectroscopy (EDX) (Fig. 8). The probed edges are  $K$  edge of O,  $L$  edges of Cr, Mn, Ge, Co, Fe, and  $M$  edge of Au. It should be noted that we do not look at the O edge in the Cr-buffer layer due to the fact that O  $K$ -edge and Cr  $L$ -edge are too close in energy. This analysis confirms the good chemical homogeneity in each layer and abrupt interfaces without intermixing.

STEM HAADF was thus performed to characterize chemical ordering in  $Mn_3Ge$  and  $Co_2FeGe$  layers as shown in Fig. 9. The [110] zone axis was preferred because our Heusler compounds has only mono-elemental columns [27] for this direction as sketched in the figure. The chemical ordering can then easily be analyzed by selecting appropriate profiles along the atomic planes stacks. The observations are in total agreement with the chemical ordering expected for the  $D0_{22}$  ( $Mn_3Ge$ ) and  $L2_1$  ( $Co_2FeGe$ ) structures.

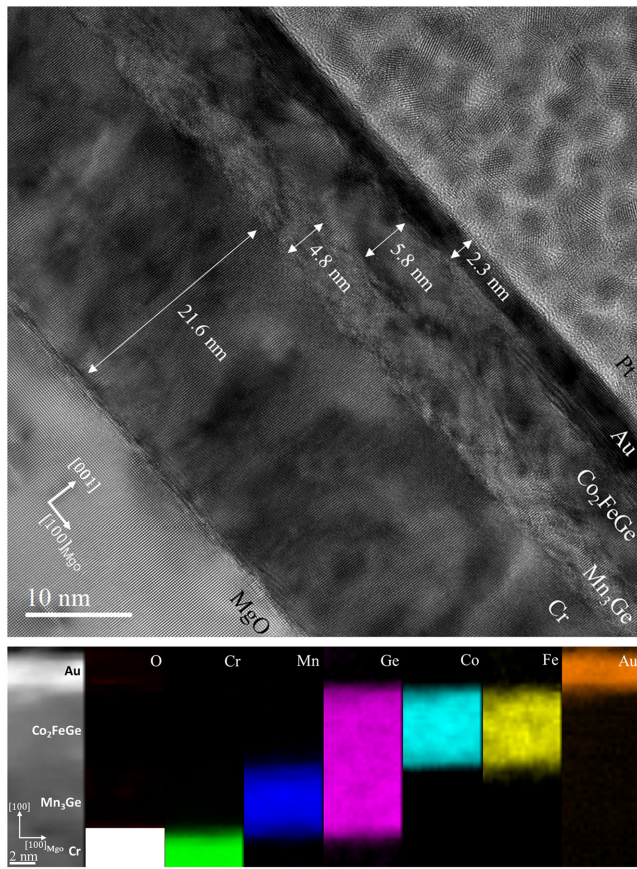


FIG. 8. Top—TEM image of MgO/Cr/Mn<sub>3</sub>Ge/Co<sub>2</sub>FeGe/Au sample. Bottom—EDX mapping of the cross section. The mapped area is shown on the left. The chemical occupation along the stack shows homogeneous concentration of the elements in each layer without intermixing.

The magnetic properties of these bilayers were analyzed using XMCD experiments performed at room temperature at Mn, Fe and Co  $L_{2,3}$  edges. The bilayers series was capped with only 2-nm-thick Au films in order to limit the x-ray absorption by the capping. The XMCD results are shown in Fig. 10. Focusing first on the absorption spectra (XAS), one may note that the Fe and Co XAS spectra are like in pure metals except for 2 and 3 nm since some multiplets appears. These multiplets may be attributed to some oxygen contamination near the Co<sub>2</sub>FeGe/Au interface due to too thin Au capping to protect the samples from air. However, a change of Co<sub>2</sub>FeGe electronic structure when decreasing the thickness down to few unit cells cannot be eliminated. We thus prepared the same sample but with a V-capping layer. As V is lighter than Au, the capping thickness can be larger (4 nm) without absorbing too much the x rays. The XAS spectra thus show no more oxidation (as can be seen for superlattices in Fig. 13). Concerning the Mn XAS, a multiplet structure is clearly visible for all the samples. This behavior is not surprising since

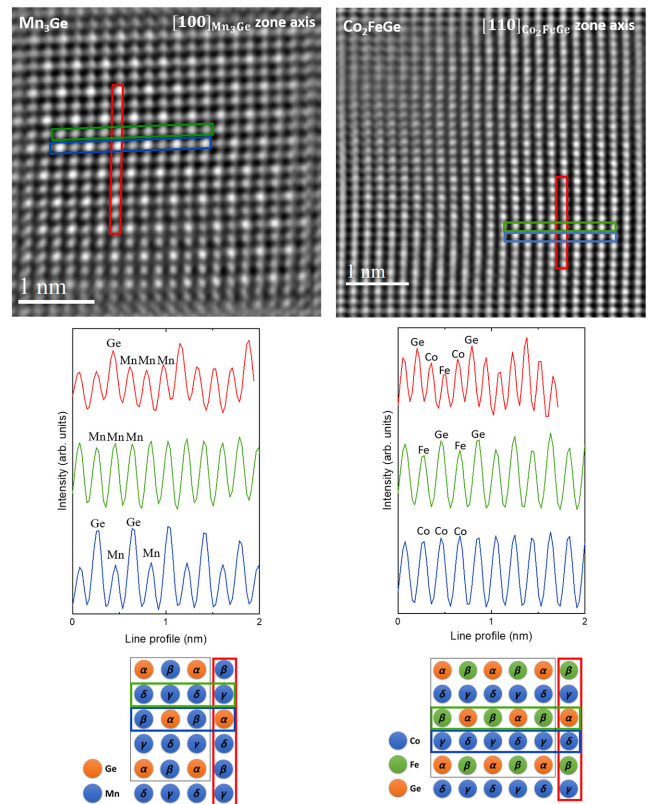


FIG. 9. From top to bottom, inverse FFT of STEM HAADF images, line profiles performed on red, green, and blue areas and expected atomic column arrangements for, respectively, the Mn<sub>3</sub>Ge D0<sub>22</sub> structure on the left and on the Co<sub>2</sub>FeGe L<sub>21</sub> structure on the right.

such multiplet structure was already observed in many Mn-based Heusler compounds and was explained to come from the special Mn hybridization with its neighbors in the cell [16,47,48]. We also observed this multiplet shape on both 50-nm-thick Mn<sub>3</sub>Ga and Mn<sub>3</sub>Ge films (see Fig. S5 within the Supplemental Material [44]).

Looking now at the XMCD in Fig. 10, a negative signal at the  $L_3$  edge and a positive one at the  $L_2$  edge were observed for the three  $L$  edges unveiling a ferromagnetic coupling between all the elements, thus between the two layers. The orbital, spin, and total magnetic moments for Co and Fe were extracted from XMCD spectra using the sum-rule analysis [49] for the Au-capped and V-capped samples (Fig. 11). It should be noted that this analysis is not pertinent for Mn due to the too small energy difference between  $L_2$  and  $L_3$  (low spin-orbit coupling). First, the impact of oxidation on the two thinnest samples covered with Au is visible with low calculated moment due to the supplementary features on the XAS spectra coming from oxidization, which show no dichroic signal. The calculated moment is more reliable on the two samples capped with V. Second, the total moment of Co and Fe

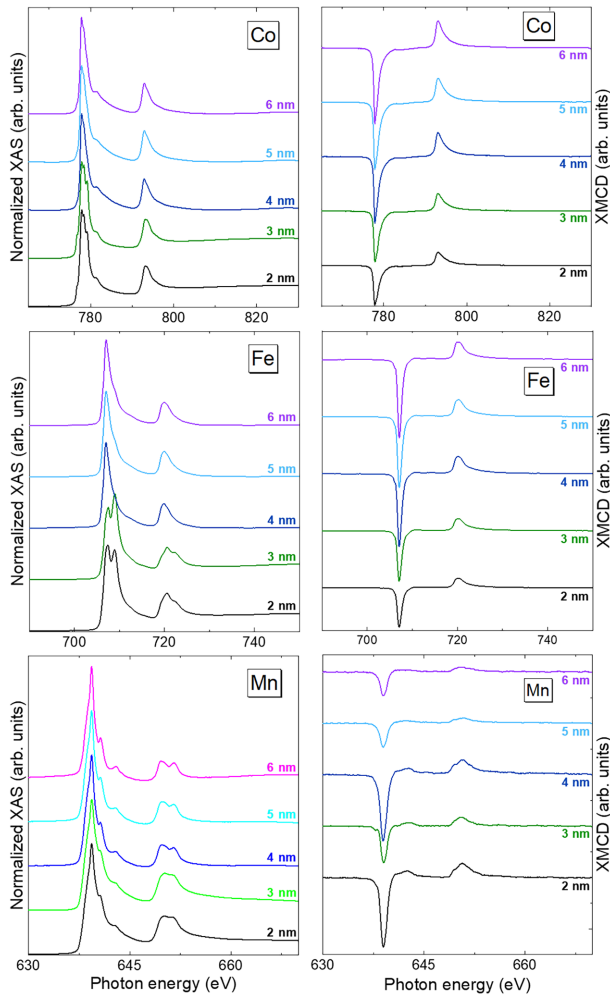


FIG. 10. XAS (on the left) and XMCD (on the right) spectra measured at  $L_{2,3}$  edges of Co, Fe and Mn. The thicknesses reported on the right of the curves stand for  $\text{Co}_2\text{FeGe}$  layer thickness.  $\text{Mn}_3\text{Ge}$  thickness is 5 nm for each sample. Measurement performed at 300 K under a 6 T magnetic field.

are close to the theoretical values for the highest  $\text{Co}_2\text{FeGe}$  thicknesses, whereas the two thinner samples, especially for Fe, displayed a reduced moment.

XMCD hysteresis loops were recorded at Fe and Mn edges with a magnetic field normal to the sample surface (Fig. 12). Similar loops were observed at the Co edge but much more noisy (Fig. S6 within the Supplemental Material [44]). As expected, the loops at Fe and Mn edges are exactly the same meaning that the two layers are coupled and behave as a unique ferromagnetic layer. If PMA was observed for all the  $\text{Co}_2\text{FeGe}$  thicknesses, a clear decreasing tendency of the out-of-plane magnetic anisotropy is observed while increasing  $\text{Co}_2\text{FeGe}$  thickness. Nonetheless, hysteresis loops obtained for low  $\text{Co}_2\text{FeGe}$  thickness show a good remanence with slightly bent cycles and are very promising for spintronic application.

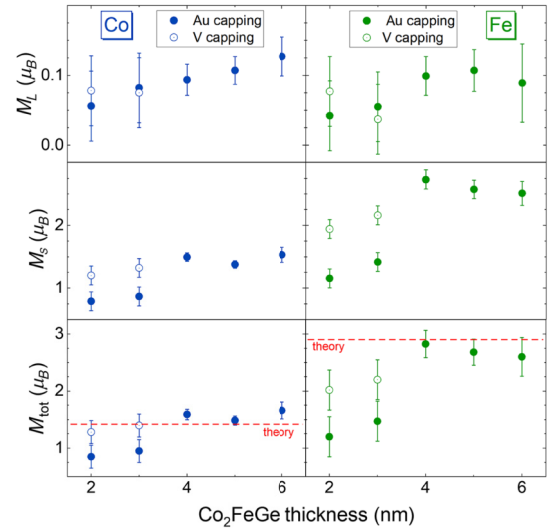


FIG. 11. From top to bottom, extracted values of orbital, spin, and total magnetic moments for Co (left) and Fe (right). Solid circles are for Au-capped samples, hollow circles are for V-capped samples. Theoretical values in red dashed lines taken from Ref. [50].  $\text{Mn}_3\text{Ge}$  thickness is 5 nm for each sample.

### B. $\text{Mn}_3\text{Ge}/\text{Co}_2\text{FeGe}$ superlattices on Cr(001)

The next step of this study was to look at the magnetic property evolution when repeating the  $\text{Mn}_3\text{Ge}/\text{Co}_2\text{FeGe}$  bilayer. It is well known that repetitions usually affect the coercive field, the remanence, and the total magnetic anisotropy of the systems [51]. Moreover, the higher magnetic volume will allow us to characterize the films by MOKE measurements.  $\text{Co}_2\text{FeGe}$  is still used here

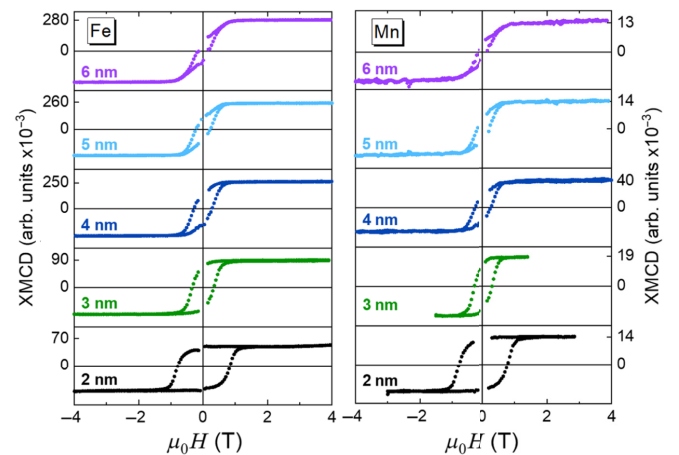


FIG. 12. XMCD hysteresis loops obtained in normal incidence at the Fe (on the left) and Mn (on the right)  $L_3$  edges with an out-of-plane applied magnetic field. From bottom to top,  $\text{Co}_2\text{FeGe}$  thickness from 2 nm to 6 nm.  $\text{Mn}_3\text{Ge}$  thickness is 5 nm for each sample. Measurements performed at 300 K.

to get separated XMCD information from the two layers. The  $\text{Mn}_3\text{Ge}$  thickness is decreased from 5 nm (in the previous bilayers) to 3 nm in order to decrease the PMA and so the coercive field since we are limited to 0.9 T in our MOKE setup. In this study, five samples were grown with the following composition:  $\text{MgO}/\text{Cr}(10 \text{ nm})/[\text{Mn}_3\text{Ge}(3 \text{ nm})/\text{Co}_2\text{FeGe}(X \text{ nm})]_{\times 5}$  with  $X = 1, 2, 3, 4,$  and  $5 \text{ nm}$ . Since 2-nm Au were not sufficient to protect the samples, as shown in the previous section, we moved to lighter materials to limit x-ray absorption from the capping and chose V (4 nm) capping layers. The RHEED patterns all over the stack growth were similar to what was observed before.

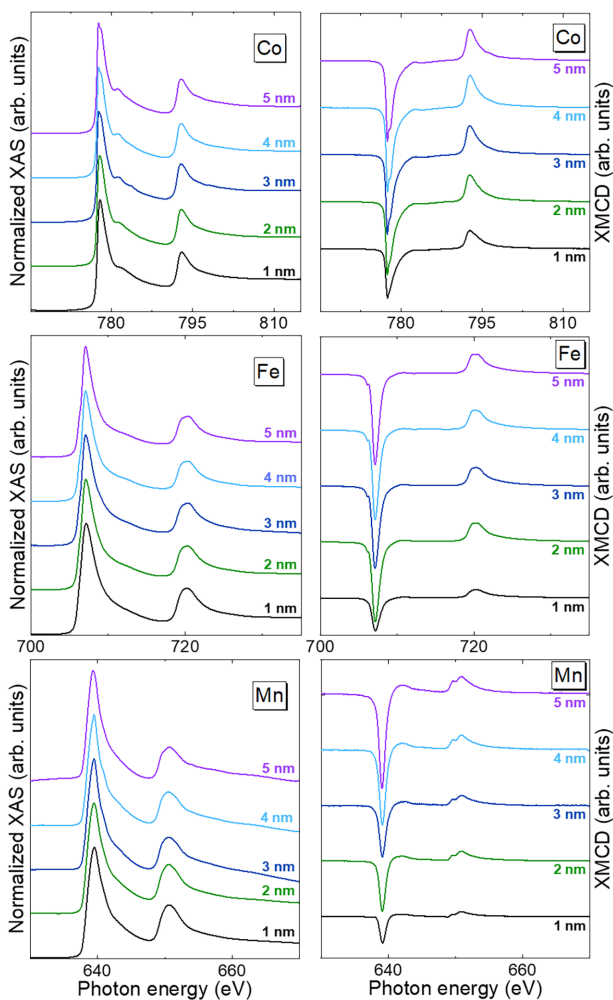


FIG. 13. XAS (left) and XMCD (right) spectra measured at  $L_{2,3}$  edges of Co, Fe, and Mn on the  $\text{Mn}_3\text{Ge}/\text{Co}_2\text{FeGe}$  superlattices series, grown on Cr-buffer layers and capped with V. The thicknesses reported on the right of the curves stand for  $\text{Co}_2\text{FeGe}$  layer thickness.  $\text{Mn}_3\text{Ge}$  thickness is 3 nm for each sample. Measurement performed at 300 K under a 6-T magnetic field.

The XAS and XMCD spectra for the whole series measured at the  $L_{2,3}$  edges of Co, Fe, and Mn are given in Fig. 13. Co and Fe transitions are similar to the ones observed in the previous section for V-capped samples. First, no oxidation is observed on Co and Fe. Second, the Mn XAS are different to what has been observed on Au-capped samples. The multiplet structure is still present but much less defined than in Fig. 10. On their side, the dichroic signals are similar to those obtained for  $\text{Mn}_3\text{Ge}/\text{Co}_2\text{FeGe}$  bilayers. The identical XMCD signs present at the  $L_3$  (negative) and  $L_2$  (positive) edges of Co, Fe, and Mn attest to the ferromagnetic exchange between the elements and layers.

Hysteresis loops were performed in normal and grazing incidences ( $20^\circ$  off normal) with the magnetic field applied along the beam direction. The resulting data measured at the Fe edge are given in Fig. 14. First, samples with  $t_{\text{Co}_2\text{FeGe}} = 1$  and  $2 \text{ nm}$  are clearly perpendicularly magnetized and the loops are square with 100% remanence. For higher  $\text{Co}_2\text{FeGe}$  thicknesses, the magnetization starts to switch in the film plane. The loops measured in grazing incidence confirm this behavior with an obvious easy axis toggling in the film plane for the thicker samples. Note that the loops opening in grazing incidence for  $t_{\text{Co}_2\text{FeGe}} = 1$  and  $2 \text{ nm}$  is not surprising since the measurements cannot be performed perfectly in plane.

Finally, spin, orbital, and total magnetic moments were extracted using the sum rules for Fe and Co (Fig. 15). Similarly to bilayers, the thinner sample depicts magnetic moments values lower than in the bulk. This is explained by the only 1-nm-thick  $\text{Co}_2\text{FeGe}$  that has still not reached its bulk values.

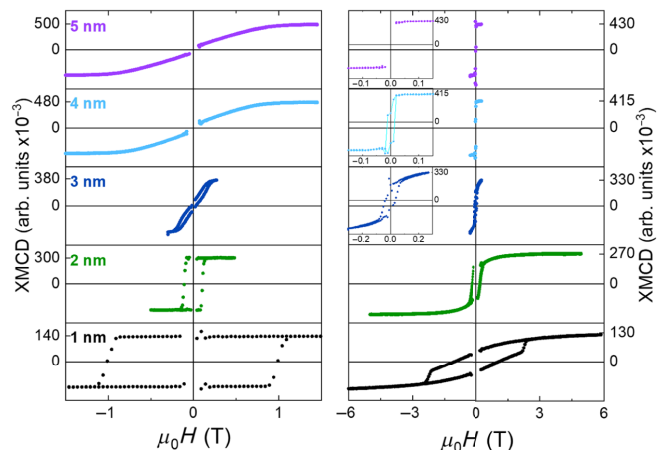


FIG. 14. XMCD hysteresis loops obtained at the Fe  $L_3$  edge with a beam applied normal to the sample surface (on the left) and applied in grazing incidence (on the right). From bottom to top, increase of the  $\text{Co}_2\text{FeGe}$  thickness from 2 to 5 nm.  $\text{Mn}_3\text{Ge}$  thickness is 3 nm for each sample. The inset graphs are enlargements of the loops. Measurements performed at 300 K.

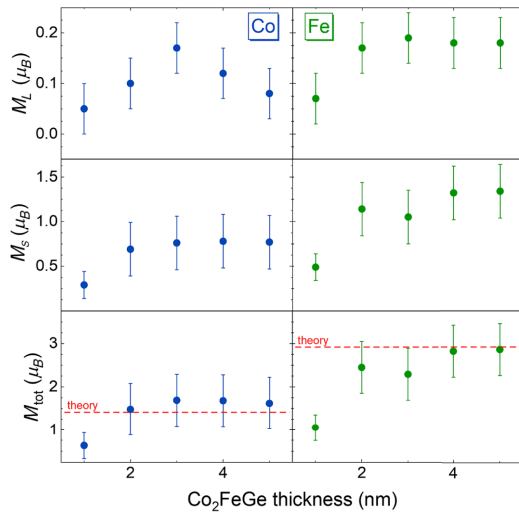


FIG. 15. Extracted values of orbital, spin, and total magnetic moments for Co (on the left) and Fe (on the right). The theoretical values, represented in red dashed lines are taken from Ref. [50]. Mn<sub>3</sub>Ge thickness is 3 nm for each sample.

## VI. PMA REPLICATION CHARACTERIZED BY *IN SITU* UHV MOKE

These kinds of samples fully characterized using XMCD were chosen to test the new MOKE setup installed on the Daum UHV tube (at least in polar configuration, that is for an applied magnetic field perpendicular to the film plane). The growth was performed on the MBE and samples were then transferred to the MOKE chamber all under UHV. The sample was placed at the center of an electromagnet that allows application of a magnetic field up to 0.9 T in the direction normal to the sample surface (Fig. S3 within the Supplemental Material [44]). There are at least three main advantages of using this technique here: the measurement is sensitive to the thin film and not to the substrate (contrary to PPMS VSM and SQUID VSM measurements). The film is measured immediately after the growth process. No capping is needed (contrary to VSM and XMCD). This gives the possibility to see any influence of the capping on the magnetic properties of the underneath magnetic layer. Finally, no diamagnetic correction due to MgO substrate and Pd buffer has to be taken into account resulting in a hysteresis loop characterizing only the superlattices.

### A. Mn<sub>3</sub>Ge/Co<sub>2</sub>FeGe to test the MOKE setup

Five samples with the following stack MgO/Cr(10 nm)/[Mn<sub>3</sub>Ge(3 nm)/Co<sub>2</sub>FeGe(*X* nm)]<sub>×5</sub> with *X* = 0.5, 1, 2, 3, and 5 nm were characterized with the MOKE setup. The resulting curves are given in Fig. 16. The first observation that jumps out is the signal inversion occurring between samples with 1 and 2 nm of Co<sub>2</sub>FeGe. This inversion is attributed to the different sign of Kerr rotation hosted by Mn<sub>3</sub>Ge and Co<sub>2</sub>FeGe. For low Co<sub>2</sub>FeGe thicknesses, the

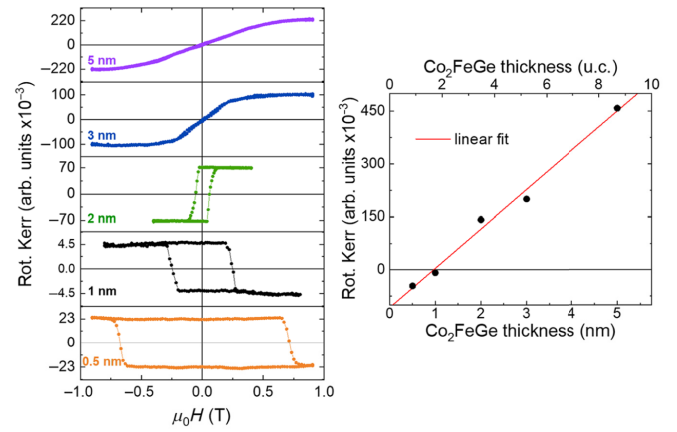


FIG. 16. On the left, MOKE hysteresis loops obtained at 300 K with an out-of-plane applied magnetic field. From bottom to top, increase of the Co<sub>2</sub>FeGe thickness from 0.5 nm to 5 nm. Mn<sub>3</sub>Ge thickness is 3 nm for each sample. On the right, Kerr rotation amplitude as a function of Co<sub>2</sub>FeGe thickness.

loop is inverted due to dominant Mn<sub>3</sub>Ge layers. As far as the Co<sub>2</sub>FeGe thickness increases, the signal vanishes and the null Kerr angle is reached between  $t_{\text{Co}_2\text{FeGe}} = 1$  and 2 nm. This behavior is clearly supported by the right graph of Fig. 16 where a linear dependence of the Kerr amplitude with Co<sub>2</sub>FeGe thickness is observed. An additional sample, made with only a Co<sub>2</sub>FeGe layer, was measured and unveiled a classical Kerr rotation sign (i.e., sign observed for  $t_{\text{Co}_2\text{FeGe}} = 2, 3,$  and 5 nm in Fig. 16) attesting to the inverse Mn<sub>3</sub>Ge Kerr rotation.

### B. Mn<sub>3</sub>Ga/Co<sub>2</sub>MnSi

Mn<sub>3</sub>Ga/Co<sub>2</sub>MnSi superlattices were first grown and measured in our UHV MOKE setup. A typical example is shown in Fig. 17 for three Mn<sub>3</sub>Ga unit cells (2.2 nm) and five Co<sub>2</sub>MnSi unit cells (2.8 nm) repeated 5 times. The open hysteresis loop confirms that the SL is perpendicularly magnetized. Nonetheless, the cycle is stretched and curved. As a consequence, a very low magnetic remanence (of the order of 18%) is obtained confirming the huge PMA even in so thin Mn<sub>3</sub>Ga films. In particular, we cannot eliminate that the stack was not saturated at 0.9 T. The huge PMA in Mn<sub>3</sub>Ga thus makes the MOKE study very difficult according to our setup facilities. These conclusions motivated us to look at the other candidate, i.e., Mn<sub>3</sub>Ge.

### C. Mn<sub>3</sub>Ge/Co<sub>2</sub>MnGe

The architecture of the samples was MgO/Cr(10 nm)/[Mn<sub>3</sub>Ge (2 u.c.)/Co<sub>2</sub>MnGe(*X* u.c.)]<sub>×5</sub> with *X* = 1, 2, 3, and 4 unit cells. The RHEED patterns observed all along the growth were similar to what we observed in the stacks shown in the previous section. As for Co<sub>2</sub>FeGe, an inversion of the Kerr rotation was observed (Fig. 18). The MOKE signal is gradually decreasing while increasing the

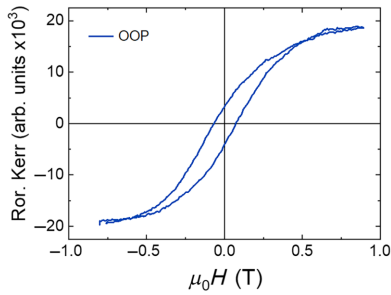


FIG. 17. Out-of-plane (OOP) hysteresis loop obtained for  $[\text{Mn}_3\text{Ga} (3 \text{ unit cells})/\text{Co}_2\text{MnSi} (5 \text{ unit cells})]_{\times 5}$  superlattice by MOKE measurement. Note the bended loop shape and low remanence.

$\text{Co}_2\text{MnGe}$  thickness. This time, the global Kerr rotation is cancelled for  $t_{\text{Co}_2\text{MnGe}}$  close to 4 unit cells. This difference in compensation point between  $\text{Co}_2\text{FeGe}$  and  $\text{Co}_2\text{MnGe}$  is not surprising since the magnetic moment per cell is larger in  $\text{Co}_2\text{FeGe}$  ( $6\mu_B$ ) than in  $\text{Co}_2\text{MnGe}$  ( $5\mu_B$ ). Similarly to  $\text{Co}_2\text{FeGe}$ ,  $\text{Co}_2\text{MnGe}$  has a classical Kerr rotation that counterbalances the inverted one of  $\text{Mn}_3\text{Ge}$  but the PMA replication is then easier. A linear relationship is also observed in the Kerr rotation amplitude versus  $\text{Co}_2\text{MnGe}$  thickness graph (Fig. 18). Our main goal, i.e., PMA replication in a HMM film with 100% remanence, is obtained in these systems.

#### D. $\text{Mn}_3\text{Ge}/\text{Co}_2\text{MnSi}$

Similar experiments were performed on samples replacing  $\text{Co}_2\text{MnGe}$  by  $\text{Co}_2\text{MnSi}$  on top of  $\text{Mn}_3\text{Ge}$ . For  $\text{Mn}_3\text{Ge}$  film thicknesses up to 4 nm (around 6 u.c.), the observed MOKE loops were very similar to those reported in Fig. 18, meaning that the  $\text{Mn}_3\text{Ge}$  and  $\text{Co}_2\text{MnSi}$  layers are ferromagnetically coupled. However, this coupling

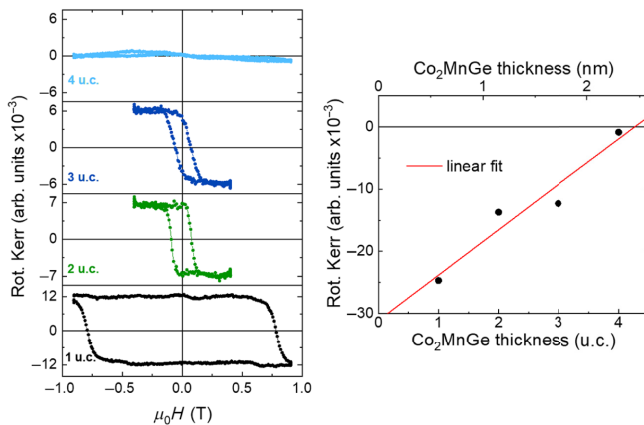


FIG. 18. On the left, MOKE out-of-plane hysteresis loops on a series of  $[\text{Mn}_3\text{Ge} (2 \text{ u.c.})/\text{Co}_2\text{MnGe} (X \text{ u.c.})]_{\times 5}$  with  $X$  noted on the inset. Measurements performed at 300 K. On the right, Kerr rotation amplitude as a function of  $\text{Co}_2\text{MnGe}$  thickness.

does not hold anymore for thicker  $\text{Mn}_3\text{Ge}$  layers (above 7 u.c. = 5 nm). Some typical MOKE loops performed on  $\text{Mn}_3\text{Ge}/\text{Co}_2\text{MnSi}$  bilayers are shown in Fig. 19. The sharp magnetization reversal comes from  $\text{Mn}_3\text{Ge}$  meaning that its magnetization is out of plane. In addition we observed a linear variation of the magnetization with the applied magnetic field coming from the coherent rotation of the  $\text{Co}_2\text{MnSi}$  magnetization from in plane at zero field to out of plane at saturation. This means that at zero field the  $\text{Mn}_3\text{Ge}$  magnetization is perpendicular to the stack whereas the  $\text{Co}_2\text{MnSi}$  one is in plane, leading to a  $90^\circ$  magnetic configuration between the two layers. Such a magnetic configuration is typical of two independent magnetic layers meaning that there is no magnetic coupling between them. However, it should be noticed that  $\text{Mn}_3\text{Z}$  in the bulk is suspected to exhibit noncolinear magnetic moments between the two nonequivalent Mn sites within the  $\text{D0}_{22}$  structure. A possible scenario is that the magnetic moment at the  $\text{Mn}_3\text{Z}$  surface is in plane and coupled to the  $\text{Co}_2\text{MnSi}$  magnetic moment, leading to a  $90^\circ$  magnetic configuration between the two layers. As the magnetic configuration between  $\text{Mn}_3\text{Ge}$  and  $\text{Co}_2\text{MnSi}$  magnetizations moves from  $0^\circ$  to  $90^\circ$  increasing  $\text{Mn}_3\text{Ge}$  thickness, this strongly suggests that the suspected noncolinear magnetic structure in bulk  $\text{Mn}_3\text{Z}$  is strongly affected in thin films and depends on its thickness.

#### VII. DISCUSSION AND CONCLUSION

This study allows us to enumerate useful conclusions on Mn-Ga and Mn-Ge thick films:

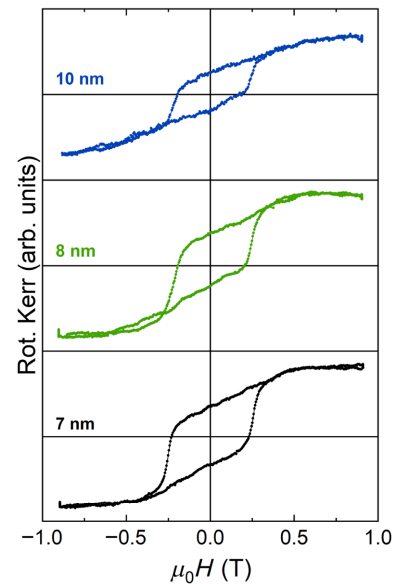


FIG. 19. MOKE out-of-plane hysteresis loops on a series of  $\text{Mn}_3\text{Ge} (5 \text{ nm})/\text{Co}_2\text{MnSi} (X \text{ nm})$  with  $X$  noted on the inset. Measurements performed at 300 K.

(i) For both alloys, we found that the 3:1 stoichiometry is the best compromise for applications in terms of low saturation magnetization, high coercive field, and high remanent magnetization.

(ii)  $\text{Mn}_3\text{Ga}$  and  $\text{Mn}_3\text{Ge}$  thin films were observed to grow in the  $\text{D0}_{22}$  structure on Pd and Cr(002) whatever the thickness of the films (up to 50 nm).

(iii) The PMA is stronger in  $\text{Mn}_3\text{Ga}$  than in  $\text{Mn}_3\text{Ge}$ .

(iv) The PMA is larger for both compounds grown on Pd- than on Cr-buffer layers. This is due to a lower misfit on Pd (better crystalline quality) than on Cr.

(v) Off stoichiometry is not a problem for the crystalline quality of Mn-Ga alloys. However, several crystalline phases coexist for Mn-Ge alloys (Ge-rich alloys).

(vi) We confirm that the magnetic state of the  $\text{Mn}_3\text{Ga}$  compound is not trivial (our results are compatible with a ferrimagnetic compensated state as proposed theoretically and experimentally). Getting squared loops with 100% remanence needed for applications is thus challenging.

(vii) The magnetic behavior of the  $\text{Mn}_3\text{Ge}$  compound is easier to manipulate and thus more suitable for devices.

(viii) The magnetization of the  $\text{Mn}_3\text{Z}$  compounds decrease for small thicknesses.

From all these conclusions one may choose both alloys, and the stoichiometry can be varied as well (but with care for Mn-Ge alloys). Furthermore, very low magnetic damping was predicted for the 3:1 stoichiometry [36] and observed to be close to  $10^{-2}$  for stoichiometric  $\text{Mn}_3\text{Ge}$  [52] and off-stoichiometric  $\text{Mn}_{1.54}\text{Ga}$  and  $\text{Mn}_{2.12}\text{Ga}$  alloys [53]. We can go as far as to say that off stoichiometry may have a great impact on the magnetic damping (different chemical ordering), as seen, for instance, in  $\text{Co}_2\text{Mn}$ -based full Heusler compounds [27].

Starting from these compounds with large PMA, a large variety of Heusler alloys can be epitaxially grown on them, as already shown by the group of Mizukami [38–42] for  $\text{Co}_2\text{MnZ}'$  ( $Z' = \text{Si}$  and  $\text{Al}$ ) and  $\text{Co}_2\text{FeZ}'$  ( $Z' = \text{Si}$  and  $\text{Al}$ ) grown on Mn-Ga alloys. We show here that same compounds with  $Z' = \text{Ge}$  can be added to the list, and it may be completed at least with  $Z' = \text{Ga}$ ,  $\text{Sn}$ , or  $\text{Sb}$ . Furthermore, a behavior has to be known for devices, i.e., the coupling between the  $\text{Mn}_3\text{Z}$  and the HMM layers. At least two groups have studied this coupling. The Mizukami group found that the coupling is ferromagnetic or antiferromagnetic. They first observed that the coupling is always ferromagnetic for thin  $\text{Mn}_3\text{Z}$  thicknesses. We found in our studied systems a similar behavior. In addition, they observed that this coupling changes to an antiferromagnetic one for thicker  $\text{Mn}_3\text{Z}$  films coupled with an annealing done after the stack growth [39,40,42]. A second group [43] also observed this antiferromagnetic coupling in  $\text{Mn}_3\text{Ga}/\text{Co}_2\text{MnSi}$  bilayers using the same annealing process. We also observed here that the coupling changes when increasing the  $\text{Mn}_3\text{Ge}$  thickness but

we never observed an AF coupling. Our results are consistent with a  $90^\circ$  magnetic configuration but one should note that we did not anneal the stacks. These results are not in contradiction since one can imagine that interfacial atomic arrangement may be strongly influenced by the annealing even if intermixing takes place over one or 2 atomic planes. To resume, it is very difficult to give clear conclusions at this stage since many parameters may change the coupling, like the respective Mn-Z and HMM stoichiometries, layers thicknesses, growth and annealing temperatures, and possible impact of C or O contamination at the interfaces (which may be very different in sputtered films in normal conditions, sputtered films in a UHV environment, or MBE grown stacks). Consequently addressing this point in order to understand in detail the coupling requires extensive research. Our study can definitely not answer in detail this question, but provides a very interesting way to control the coupling in these systems through interface engineering.

The MOKE analysis of these stacks allowed us to evidence a very special feature: we clearly observed that the Kerr rotations are in opposite direction between, on one side,  $\text{Mn}_3\text{Ga}$  and  $\text{Mn}_3\text{Ge}$ , and on the other side, the different HMM films studied here, i.e.,  $\text{Co}_2\text{FeGe}$ ,  $\text{Co}_2\text{MnGe}$  and  $\text{Co}_2\text{MnSi}$ . The origin of such optical behavior is not established here but it clearly explains the MOKE hysteresis loops observed by Ranjbar *et al.* [40]. Indeed, they observed a total Kerr rotation lower when the Mn-Z and HMM are ferromagnetically coupled than when these two layers are antiferromagnetically coupled. These opposite Kerr rotations are thus also present in Mn-Z/ $\text{Co}_2\text{FeAl}$ ,  $\text{Co}_2\text{FeSi}$ , and  $\text{Co}_2\text{MnAl}$  stacks.

To summarize, the strong PMA in Mn-Ga and Mn-Ge tetragonal  $\text{D0}_{22}$  phase can be used to get HMM films with perpendicular anisotropy. Numerous Mn-Z and HMM combinations are possible due to a very good matching between the lattice along the (001) direction. Based on our results thin  $\text{Mn}_3\text{Ge}$  films on Cr or Pd(001) may be preferred for spintronic applications. The global magnetic behaviors, like remanence, saturation magnetization, coercive fields, can be easily engineered according to device constraints. Finally, the very small magnetization of the Mn-Z films combined with PMA and ultralow magnetic damping may significantly improve device performance by reducing energy consumption for instance.

## ACKNOWLEDGMENTS

The work was partially funded by the French National Research Agency (ANR) through Project ANR-20-CE24-0012-07 “Marin-ANR.” Samples in the present study were prepared and characterized at Institut Jean Lamour’s UHV Daum tube. The authors thank CRYOSCAN for technical



support on the UHV MOKE. These facilities are partially funded by FEDER and Grand Est region through the RANGE project. XAS and XMCD measurements at ALBA BL29 Boreas beamline were performed via Proposals No. 2021024919 and No. 2022015556.

- [1] R. de Groot, F. M. Mueller, P. G. van Engen, and K. H. J. Buschow, New class of materials: Half-metallic ferromagnets, *Phys. Rev. Lett.* **50**, 2024 (1983).
- [2] I. Galanakis, *Theory of Heusler and Full-Heusler Compounds*, edited by C. Felser and A. Hirohata (Springer, Cham., 2016).
- [3] M. Jourdan, J. Minár, J. Braun, A. Kronenberg, S. Chadov, B. Balke, A. Gloskovskii, M. Kolbe, H. J. Elmers, G. Schönhense, H. Ebert, C. Felser, and M. Kläui, Direct observation of half-metallicity in the Heusler compound  $\text{Co}_2\text{MnSi}$ , *Nat. Commun.* **5**, 4974 (2014).
- [4] S. Andrieu, A. Neggache, T. Hauet, T. Devolder, A. Hallal, M. Chshiev, A. Bataille, P. Le Fèvre, and F. Bertran, Direct evidence for minority spin gap in the  $\text{Co}_2\text{MnSi}$  Heusler compound, *Phys. Rev. B* **93**, 094417 (2016).
- [5] C. Guillemard, S. Petit-Watelot, L. Pasquier, D. Pierre, J. Ghanbaja, J. C. Rojas-Sánchez, A. Bataille, J. Rault, P. Le Fèvre, F. Bertran, and S. Andrieu, Ultralow magnetic damping in  $\text{Co}_2\text{Mn}$ -based Heusler compounds: Promising materials for spintronics, *Phys. Rev. Appl.* **11**, 064009 (2019).
- [6] C. Guillemard, W. Zhang, G. Malinowski, C. D. Melo-Sanchez, J. Gorchon, S. Petit-Watelot, J. Ghanbaja, S. Mangin, P. L. Fèvre, F. Bertran, and S. Andrieu, Engineering  $\text{Co}_2\text{MnAl}_x\text{Si}_{1-x}$  Heusler compounds as a model system to correlate spin polarization, intrinsic Gilbert damping and ultrafast demagnetization, *Adv. Mater.* **32**, 1908357 (2020).
- [7] S. V. Faleev, Y. Ferrante, J. Jeong, M. G. Samant, B. Jones, and S. S. P. Parkin, Origin of the tetragonal ground state of Heusler compounds, *Phys. Rev. Appl.* **7**, 034022 (2017).
- [8] D. Zhang, B. Yan, S. C. Wu, J. Kübler, G. Kreiner, S. S. P. Parkin, and C. Felser, First-principles study of the structural stability of cubic, tetragonal and hexagonal phases in  $\text{Mn}_3\text{Z}$  ( $\text{Z}=\text{Ga}$ ,  $\text{Sn}$  and  $\text{Ge}$ ) Heusler compounds, *J. Phys. Condens. Matter* **25**, 206006 (2013).
- [9] H. Kurt, N. Baadji, K. Rode, M. Venkatesan, P. Stamenov, S. Sanvito, and J. M. D. Coey, Magnetic and electronic properties of  $D_{22}\text{-Mn}_3\text{Ge}$  (001) films, *Appl. Phys. Lett.* **101**, 132410 (2012).
- [10] T. Chen, J. Wang, Z. Cheng, X. Wang, and H. Chen, Structural, electronic and magnetic properties of  $\text{Mn}_x\text{Ga}/\text{Co}_2\text{MnSi}$  ( $x = 1, 3$ ) bilayers, *Sci. Rep.* **8**, 16530 (2018).
- [11] B. S. Yang, L. N. Jiang, W. Z. Chen, P. Tang, J. Zhang, X. G. Zhang, Y. Yan, and X. F. Han, First-principles study of perpendicular magnetic anisotropy in ferrimagnetic  $D_{22}\text{-Mn}_3\text{X}$  ( $\text{X} = \text{Ga}$ ,  $\text{Ge}$ ) on  $\text{MgO}$  and  $\text{SrTiO}_3$ , *Appl. Phys. Lett.* **112**, 142403 (2018).
- [12] E. Krén and G. Kádár, Neutron diffraction study of  $\text{Mn}_3\text{Ga}$ , *J. Appl. Phys.* **8**, 1653 (1970).
- [13] B. Balke, G. H. Fecher, J. Winterlik, and C. Felser,  $\text{Mn}_3\text{Ga}$ , a compensated ferrimagnet with high Curie temperature and low magnetic moment for spin torque transfer applications, *Appl. Phys. Lett.* **90**, 152504 (2007).
- [14] J. Winterlik, B. Balke, G. Fecher, C. Felser, M. C. M. Alves, F. Bernardi, and J. Morais, Structural, electronic, and magnetic properties of tetragonal  $\text{Mn}_{3-x}\text{Ga}$ : Experiments and first-principles calculations, *Phys. Rev. B* **77**, 054406 (2008).
- [15] H. Kurt, K. Rode, M. Venkatesan, P. Stamenov, and J. M. D. Coey, High spin polarization in epitaxial films of ferrimagnetic  $\text{Mn}_3\text{Ga}$ , *Phys. Rev. B* **83**, 020405 (2011).
- [16] K. Rode, N. Baadji, D. Betto, Y. C. Lau, M. Venkatesan, P. Stamenov, S. Sanvito, J. M. D. Coey, F. Porcher, and G. André, Site-specific order and magnetism in tetragonal  $\text{Mn}_3\text{Ga}$  thin films, *Phys. Rev. B* **87**, 184429 (2013).
- [17] H. Lee, H. Sukegawa, J. Liu, S. Mitani, and K. Hono, Tuning the magnetic properties and surface morphology of  $D_{22}\text{Mn}_{3.3}\text{Ga}$  films with high perpendicular magnetic anisotropy by N doping, *Appl. Phys. Lett.* **109**, 152402 (2016).
- [18] X. P. Zhao, J. Lu, S. W. Mao, Z. F. Yu, D. H. Wei, and J. H. Zhao, Spin-orbit torque induced magnetization switching in ferrimagnetic Heusler alloy  $D_{22}\text{-Mn}_3\text{Ga}$  with large perpendicular magnetic anisotropy, *Appl. Phys. Lett.* **115**, 142405 (2019).
- [19] A. Sugihara, S. Mizukami, Y. Yamada, K. Koike, and T. Miyazaki, High perpendicular magnetic anisotropy in  $D_{22}\text{-Mn}_{3+x}\text{Ge}$  tetragonal Heusler alloy films, *Appl. Phys. Lett.* **104**, 132404 (2014).
- [20] A. Sugihara, K. Z. Suzuki, T. Miyazaki, and S. Mizukami, Magnetic properties of ultrathin tetragonal Heusler  $D_{22}\text{-Mn}_3\text{Ge}$  perpendicular-magnetized films, *J. Appl. Phys.* **117**, 17B511 (2015).
- [21] J. Jeong, Y. Ferrante, S. V. Faleev, M. G. Samant, C. Felser, and S. S. P. Parkin, Termination layer compensated tunnelling magnetoresistance in ferrimagnetic Heusler compounds with high perpendicular magnetic anisotropy, *Nat. Commun.* **7**, 10276 (2016).
- [22] J. Seyd, I. Pilottek, N. Y. Schmidt, O. Caha, M. Urbanek, and M. Albrecht,  $\text{Mn}_3\text{Ge}$ -based tetragonal Heusler alloy thin films with addition of Ni, Pt, and Pd, *J. Phys.: Condens. Matter* **32**, 145801 (2020).
- [23] A. Kobayashi, T. Higo, S. Nakatsuji, and Y. Otani, Structural and magnetic properties of  $\text{Mn}_3\text{Ge}$  films with Pt and Ru seed layers, *AIP Adv.* **10**, 015225 (2020).
- [24] X. Wang, C. Zhang, Q. Yang, L. Liu, D. Pan, X. Chen, J. Deng, T. Zhai, and H. X. Deng, Manipulation of crystalline structure, magnetic performance, and topological feature in  $\text{Mn}_3\text{Ge}$  films, *APL Mater.* **9**, 111107 (2021).
- [25] L. Ren, L. Liu, X. Shu, W. Lin, P. Yang, J. Chen, and K. L. Teo, Spin-orbit torque switching of a high-quality perpendicularly magnetized ferrimagnetic Heusler  $\text{Mn}_3\text{Ge}$  film, *ACS Appl. Mater. Interfaces* **13**, 18294 (2021).
- [26] Y. Ferrante, J. Jeong, R. Saha, S. V. Faleev, M. G. Samant, T. Topuria, H. Deniz, and S. S. P. Parkin, Tetragonal  $\text{Mn}_3\text{Sn}$  Heusler films with large perpendicular magnetic anisotropy deposited on metallic  $\text{MnN}$  underlayers using amorphous substrates, *APL Mater.* **7**, 031103 (2019).
- [27] C. Guillemard, S. Petit-Watelot, T. Devolder, L. Pasquier, P. Boulet, S. Migot, J. Ghanbaja, F. Bertran, and S. Andrieu, Issues in growing Heusler compounds in thin films for spintronic applications, *J. Appl. Phys.* **128**, 241102 (2020).

- [28] S. Wurmehl, H. C. Kandpal, G. H. Fecher, and C. Felser, Valence electron rules for prediction of half-metallic compensated-ferrimagnetic behaviour of Heusler compounds with complete spin polarization, *J. Phys.: Condens. Matter* **18**, 6171 (2006).
- [29] J. T. Holguín-momaca, C. J. Muñoz-carnero, H. Sharma, and C. R. Santillan-Rodriguez, Tuning the ferromagnetism of epitaxial-strained  $D0_{19}$ - $Mn_3Ga$  thin films, *J. Magn. Magn. Mater.* **471**, 329 (2019).
- [30] J. M. Taylor, A. Markou, E. Lesne, P. K. Sivakumar, C. Luo, F. Radu, P. Werner, C. Felser, and S. S. P. Parkin, Anomalous and topological Hall effects in epitaxial thin films of the noncollinear antiferromagnet  $Mn_3Sn$ , *Am. Phys. Soc.* **101**, 094404 (2020).
- [31] F. Wu, S. Mizukami, D. Watanabe, H. Naganuma, M. Oogane, Y. Ando, and T. Miyazaki, Epitaxial  $Mn_{2.5}Ga$  thin films with giant perpendicular magnetic anisotropy for spintronic devices, *Appl. Phys. Lett.* **94**, 122503 (2009).
- [32] S. Mizukami, T. Kubota, F. Wu, X. Zhang, T. Miyazaki, H. Naganuma, M. Oogane, A. Sakuma, and Y. Ando, Composition dependence of magnetic properties in perpendicularly magnetized epitaxial thin films of Mn-Ga alloys, *Phys. Rev. B* **85**, 014416 (2012).
- [33] E. Arras, D. Caliste, T. Deutsch, F. Lançon, and P. Pochet, Phase diagram, structure, and magnetic properties of the Ge-Mn system: A first-principles study, *Phys. Rev. B* **83**, 174103 (2011).
- [34] T. Ohoyama, K. Yasukochi, and K. Kanematsu, A new phase of an intermetallic compound  $Mn_{3,4}Ge$  and its magnetism, *J. Phys. Soc. Jpn.* **16**, 352 (1961).
- [35] G. Kádár and E. Krén, Neutron diffraction study of  $Mn_3Ge$ , *Int. J. Magn.* **1**, 143 (1971).
- [36] S. Mizukami, A. Sakuma, A. Sugihara, T. Kubota, Y. Kondo, H. Tsuchiura, and T. Miyazaki, Tetragonal  $D0_{22}Mn_{3+x}Ge$  epitaxial films grown on  $MgO(100)$  with a large perpendicular magnetic anisotropy, *Appl. Phys. Express* **6**, 123002 (2013).
- [37] T. Kubota, Y. Miura, D. Watanabe, S. Mizukami, F. Wu, H. Naganuma, X. Zhang, M. Oogane, M. Shirai, Y. Ando, and T. Miyazaki, Magnetoresistance effect in tunnel junctions with perpendicularly magnetized  $D0_{22}$ - $Mn_{3-\delta}Ga$  electrode and  $MgO$  barrier, *Appl. Phys. Express* **4**, 043002 (2011).
- [38] Q. L. Ma, X. M. Zhang, T. Miyazaki, and S. Mizukami, Artificially engineered Heusler ferrimagnetic superlattice exhibiting perpendicular magnetic anisotropy, *Sci. Rep.* **5**, 7863 (2015).
- [39] R. Ranjbar, K. Suzuki, A. Sugihara, Q. L. Ma, X. M. Zhang, T. Miyazaki, Y. Ando, and S. Mizukami, Interfacial exchange coupling in cubic Heusler  $Co_2FeZ$  ( $Z = Al$  and  $Si$ )/tetragonal  $Mn_3Ga$  bilayers, *J. Appl. Phys.* **117**, 17A332 (2015).
- [40] R. Ranjbar, K. Suzuki, A. Sugihara, Q. L. Ma, X. M. Zhang, Y. Ando, T. Miyazaki, and S. Mizukami, Structural and magnetic properties of cubic and tetragonal Heusler alloy bilayers, *Mater. Des.* **96**, 490 (2016).
- [41] R. Ranjbar, K. Z. Suzuki, A. Sugihara, Y. Ando, T. Miyazaki, and S. Mizukami, Thickness dependencies of structural and magnetic properties of cubic and tetragonal Heusler alloy bilayer films, *J. Magn. Magn. Mater.* **433**, 195 (2017).
- [42] R. Ranjbar, K. Suzuki, A. Sugihara, Q. L. Ma, X. M. Zhang, T. Miyazaki, Y. Ando, and S. Mizukami, Antiferromagnetic coupling in perpendicularly magnetized cubic and tetragonal Heusler bilayers, *Mater. Lett.* **160**, 88 (2015).
- [43] S. Mao, J. Lu, X. Zhao, X. Wang, D. Wei, J. Liu, J. Xia, and J. Zhao, MnGa-based fully perpendicular magnetic tunnel junctions with ultrathin  $Co_2MnSi$  interlayers, *Sci. Rep.* **7**, 43064 (2017).
- [44] See Supplemental Material at <http://link.aps.org/supplemental/10.1103/PhysRevApplied.20.054017>.
- [45] P. Turban, L. Hennet, and S. Andrieu, In-plane lattice spacing oscillatory behaviour during the two-dimensional hetero- and homoepitaxy of metals, *Surf. Sci.* **446**, 241 (2000).
- [46] C. Guillemand, Ph.D. thesis, Université de Lorraine (2019).
- [47] S. Seong, E. Lee, H. Kim, Y. Kim, J. Baik, and J. Kang, XMCD and PES study of a compensated-ferrimagnetic half-metal  $Mn_3Ga$ , *Curr. Appl. Phys.* **18**, 1190 (2018).
- [48] J. Okabayashi, Y. Miura, Y. Kota, K. Suzuki, A. Sakuma, and S. Mizukami, Detecting quadrupole: A hidden source of magnetic anisotropy for Manganese alloys, *Sci. Rep.* **10**, 9744 (2020).
- [49] C. T. Chen, Y. U. Idzerda, H.-J. Lin, N. V. Smith, G. Meigs, E. Chaban, G. H. Ho, E. Pellegrin, and F. Sette, Experimental confirmation of the x-ray magnetic circular dichroism sum rules for iron and cobalt, *Phys. Rev. Lett.* **75**, 152 (1995).
- [50] H. Kandpal, G. Fecher, and C. Felser, Calculated electronic and magnetic properties of the half-metallic, transition metal based Heusler compounds, *J. Phys. D: Appl. Phys.* **40**, 1507 (2007).
- [51] L. You, R. Sousa, S. Bandiera, B. Rodmacq, and B. Dieny, Co/Ni multilayers with perpendicular anisotropy for spintronic device applications, *Appl. Phys. Lett.* **100**, 172411 (2012).
- [52] S. Mizukami, A. Sugihara, S. Iihama, Y. Sasaki, K. Z. Suzuki, and T. Miyazaki, Laser-induced THz magnetization precession for a tetragonal Heusler-like nearly compensated ferrimagnet, *Appl. Phys. Lett.* **108**, 012404 (2016).
- [53] S. Mizukami, F. Wu, A. Sakuma, J. Walowski, D. Watanabe, T. Kubota, X. Zhang, H. Naganuma, M. Oogane, Y. Ando, and T. Miyazaki, Long-lived ultrafast spin precession in manganese alloys films with a large perpendicular magnetic anisotropy, *Phys. Rev. Lett.* **106**, 117201 (2011).